Advances in Water Resources 99 (2017) 15–37

Contents lists available at ScienceDirect

Advances in Water Resources

journal homepage: www.elsevier.com/locate/advwatres

A comparison of Eulerian and Lagrangian transport and non-linear reaction algorithms

David A. Benson[a,*], Tomás Aquino[b], Diogo Bolster[b], Nicholas Engdahl[c], Christopher V. Henri[d], Daniel Fernàndez-Garcia[d]

[a] Hydrological Science and Engineering, Colorado School of Mines, Golden, CO 80401, USA
[b] Civil and Environmental Engineering, University of Notre Dame, Notre Dame, IN 46556, USA
[c] Civil and Environmental Engineering, Washington State University, Pullman WA 99164, USA
[d] Department of Geotechnical Engineering and Geosciences, Universitat Politècnica de Catalunya, Barcelona, Spain

ARTICLE INFO

Article history:
Received 24 June 2014
Revised 31 October 2016
Accepted 3 November 2016
Available online 9 November 2016

MSC:
02.50.Ey
02.50.Ga
02.70.Ns
05.10.Gg,

Keywords:
Particle tracking
Chemical reaction
Numerical dispersion
Nonlinear amplification

ABSTRACT

When laboratory-measured chemical reaction rates are used in simulations at the field-scale, the models typically overpredict the apparent reaction rates. The discrepancy is primarily due to poorer mixing of chemically distinct waters at the larger scale. As a result, realistic field-scale predictions require accurate simulation of the degree of mixing between fluids. The Lagrangian particle-tracking (PT) method is a now-standard way to simulate the transport of conservative or sorbing solutes. The method's main advantage is the absence of numerical dispersion (and its artificial mixing) when simulating advection. New algorithms allow particles of different species to interact in nonlinear (e.g., bimolecular) reactions. Therefore, the PT methods hold a promise of more accurate field-scale simulation of reactive transport because they eliminate the masking effects of spurious mixing due to advection errors inherent in grid-based methods. A hypothetical field-scale reaction scenario is constructed and run in PT and Eulerian (finite-volume/finite-difference) simulators. Grid-based advection schemes considered here include 1st- to 3rd-order spatially accurate total-variation-diminishing flux-limiting schemes, both of which are widely used in current transport/reaction codes. A homogeneous velocity field in which the Courant number is everywhere unity, so that the chosen Eulerian methods incur no error when simulating advection, shows that both the Eulerian and PT methods can achieve convergence in the L^1 (integrated concentration) norm, but neither shows stricter pointwise convergence. In this specific case with a constant dispersion coefficient and bimolecular reaction $A + B \rightarrow P$, the correct total amount of product is $0.221M_{A0}$, where M_{A0} is the original mass of reactant A. When the Courant number drops, the grid-based simulations can show remarkable errors due to spurious over- and under-mixing. In a heterogeneous velocity field (keeping the same constant and isotropic dispersion), the PT simulations show an increased reaction total from $0.221M_{A0}$ to $0.372M_{A0}$ due to fluid deformation, while the 1st-order Eulerian simulations using $\approx 10^6$ cells (with a classical grid Peclet number $\Delta x/\alpha_L$ of 10) have total product of $0.53M_{A0}$, or approximately twice as much additional reaction due to advection error. The 3rd-order TVD algorithm fares better, with total product of $0.394M_{A0}$, or about 1.14 times the increased reaction total. A very strict requirement on grid Peclet numbers for Eulerian simulations will be required for realistic reactions because of their nonlinear nature. We analytically estimate the magnitude of the effect for the end-member cases of very fast and very slow reactions and show that in either case, the mass produced is proportional to $1/\sqrt{Pe}$, where Pe is the Peclet number. Therefore, extra mass is produced according to $\sqrt{D}$, where the dispersion includes any numerical dispersion error. We test two PT methods, one that kills particles upon reaction and another that decrements a particle's mass. For the bimolecular reaction studied here, the computational demands of the particle-killing methods are much smaller than, and the particle-number-preserving algorithm are on par with, the fastest Eulerian methods.

1. Introduction

Chemical reactions occur ubiquitously at a multitude of scales in hydrologic and hydrogeologic environments. A common observation is that reactions progress at lower rates at larger scales.

* Corresponding author.
E-mail addresses: dbenson@mines.edu (D.A. Benson), tomas.c.aquino@gmail.com, dbolster@nd.edu (D. Bolster), nick.engdahl@wsu.edu (N. Engdahl), christopher.henri@upc.edu, daniel.fernandez.g@upc.edu (D. Fernàndez-Garcia).

http://dx.doi.org/10.1016/j.advwatres.2016.11.003
0309-1708/

Imperfect mixing is an important contributor to the various processes that contribute to the scaling of reaction rates (Dentz et al., 2011). Mixing is the fundamental process that brings reactants into contact with one another and accurate simulations of mixing are key to correctly predicting reactions (De Simoni et al., 2005; 2007; Gramling et al., 2002). Recent studies of mixing in heterogeneous hydrologic systems demonstrate that complex rate changes can emerge, and simple assumptions about upscaled rates have been shown to lack realism (Bolster et al., 2011b; Burchard and Rennau, 2008; Chiogna et al., 2012; Le Borgne et al., 2010; Le Borgne et al., 2011; Le Borgne et al., 2013). While most of these studies have focused on mixing of conservative solutes (and/or instantaneous reactions), the results have broad implications for all mixing-driven and rate-limited reactions (Chiogna et al., 2012; De Simoni et al., 2005; 2007). Many numerical and experimental studies have shown that governing equations or numerical models that do not adequately simulate mixing will also suffer error in ultimately predicting chemical reactions (de Anna et al., 2014; 2013; Ding et al., 2012; Gramling et al., 2002; Porta et al., 2016; Sanchez-Vila et al., 2010).

Many numerical approaches exist for modeling transport of *non-reactive* solutes through heterogeneous porous media. A recent paper (Boso et al., 2013) focuses on five currently popular schemes. Broadly speaking, these authors conclude that, because of spurious numerical dispersion, the grid-based Eulerian schemes overestimate dilution/mixing, while Lagrangian approaches, including both random walk particle tracking (RWPT) and Smoothed Particle Hydrodynamics (SPH) approaches, given a sufficiently resolved and smooth velocity field, are free of numerical dispersion. The authors report that SPH is relatively computationally demanding and does not readily handle anisotropic dispersion (Avesani et al., 2015). Furthermore, the discrete nature of RWPT can lead to discontinuous concentrations, although a variety of novel algorithms have evolved in recent years to remove such spurious fluctuations (Fernàndez-Garcia and Sanchez-Vila, 2011; Pedretti and Fernàndez-Garcia, 2013). While the errors associated with these methods for non-reactive solutes are well known, the complicating factor of nonlinear reactions (which may amplify these errors), has been recognized but only qualitatively reported (Cirpka et al., 1999). In this paper, we take a more quantitative look at the difference between several widely-used Eulerian (grid-based) and Lagrangian reactive transport algorithms. For reactive transport, grid-based methods – including finite-element, finite-volume, and finite-difference – continue to largely be the norm, although there have been significant recent advances in Lagrangian approaches (Benson and Meerschaert, 2008; Bolster et al., 2016; Edery et al., 2009; Tartakovsky et al., 2007; 2008). Here we will focus on classical finite-volume/finite-difference Eulerian methods and the purely Lagrangian PT advection-dispersion-reaction schemes.

Regarding the widespread use of grid-based codes, we highlight a few approaches and recent studies. More detailed descriptions are given by Steefel et al. (2014). While different in their underlying numerical method (finite-volume, finite-element, integrated finite-difference, etc.), PFLOTRAN (Lichtner et al., 2013), TOUGHREACT (Xu et al., 2014), HYDROGEOCHEM (Yeh et al., 2004), FEHM (Zyvoloski, 1997) and NUFT (Nitao, 2000) use a 1st-order spatially accurate ($\mathcal{O}(\Delta x)$) upwind advection scheme (although NUFT allows an iterative scheme to improve accuracy (Smolarkiewicz, 1984)). The TOUGH and TOUGHREACT family of codes is routinely used to simulate CO_2 injection and reaction (e.g., Oldenburg et al., 2009; Audigane et al., 2007). Hammond and Lichtner (2010) use PFLOTRAN to simulate Uranium transport and speciation on the several-kilometer scale. Navarre-Sitchler et al. (2013) use PFLOTRAN, and Keating et al. (2013) use FEHM to simulate the release of metals and Uranium, respectively, from CO_2-acidified aquifers. None of these studies specify values for dispersivity or diffusivity, so it is likely that the authors rely on numerical error, which is a function of discretization and local velocity, to emulate real dispersion. Regardless of which code is selected, the effects of realistic dispersion on reaction are often ignored and the fastest and least accurate transport algorithm is used (Johnson et al., 2004). Steefel (2009) and White and Oostrom (1997) recognize the importance of spurious dispersion and mixing (particularly transverse to flow) on reactions and implement a 2^{nd}-order accurate variant of Leonard's (Datta-Gupta et al., 1991; Leonard, 1991) 3rd-order total-variation-diminishing (TVD) scheme. However, these codes use a 1st-order upwind scheme when the simultaneous implicit reaction and transport option is chosen. Finally, reaction algorithms (i.e., PHT3D (Barry et al., 2002; Prommer et al., 2002)) based on transport in the MT3DMS code (Zheng and Wang, 1999) may choose among several advection schemes including 1st and 3rd-order ($\mathcal{O}(\Delta x^3)$) TVD algorithms. One may also choose a mixed Lagrangian/Eulerian scheme in which advection is performed by particles and dispersion/reaction are performed on a grid after mapping particle masses back into gridded concentrations similar to the scheme by Tompson and Dougherty (1992). It is notable that Prommer et al. (2002) compare the strictly Eulerian methods to the hybrid Lagrangian/Eulerian advection/dispersion scheme in MT3DMS and find that this Lagrangian/Eulerian scheme is superior to the 3rd-order Eulerian scheme in MT3DMS. Those authors recommend the use of particle-tracking for advection as a general rule, and a similar conclusion was reached by Herrera et al. (2010) with their SPH model.

While more accurate (higher order) grid-based advection schemes have been developed (see, e.g., (Toro, 2009)), including the weighted essentially non-oscillatory (WENO) and advection-diffusion-reaction (ADER) families of methods, they have not been widely adopted in studies of aquifer geochemical reactions. One possible reason is the relatively complex nature of these methods, which reconstruct (interpolate) the profiles of the advected quantities using nth-order polynomials. The polynomials can be analytically advected with $(n+1)$th-order accuracy in 1-d, but the construction process is somewhat complicated and a matter of choice. Moving the methods to multi-dimensions is also tricky, because maintaining high-order accuracy requires an algorithm that looks in all directions (not simply a combination of 1-D sweeps) (LeVeque, 2002; LeVeque, 2005; Toro, 2009). The higher-order polynomial reconstruction can be extended to arbitrary-order polynomial basis functions in finite-element implementations (Ayuso and Marini, 2009; Cockburn and Shu, 1998; Lv and Ihme, 2014) with analogous results to the WENO finite volume algorithms (e.g., Kuzmin, 2010). A further complication to many higher-order methods is the potential for negative concentration oscillations and/or mass balance errors when spurious negative masses are quashed. Another method used to increase accuracy uses adaptive grid refinement to decrease grid size in areas of large concentration gradients (e.g., (Constantinescu et al., 2008; Mansell et al., 2002; Wolfsberg and Freyberg, 1994)). These and other efforts to improve the efficiency, accuracy, and parallel implementation of Eulerian methods for advective flux continue (e.g., Ketcheson et al., 2013; Huang et al., 2015). But the situation remains that 1st- through 3rd- order accurate, directionally split, upstream weighting is the prevailing solution method in aquifer transport and reaction studies; therefore, we investigate these schemes.

One issue with the various Eulerian implementations in that artificial mixing is exacerbated by low Courant numbers (low velocities). As a result, the artificial dispersion in the transverse, low-velocity direction can be as great as either the spurious or real dispersion in the longitudinal direction. This spurious transverse mixing is responsible for overestimating reactions for many boundary value problems (Cirpka et al., 1999). To address this problem, Cirpka et al. (1999) developed a gridding-along-streamlines ap-

proach. In 2-*d* the streamlines can be solved analytically, but in 3-*d*, particles must be used to trace streamlines or streamtubes in the areas of interest. The domain is re-discretized along streamlines so that advective fluxes do not cross cells in the transverse direction. Solving dispersion and reaction is then either done on the Eulerian grid, or the particles used to trace streamlines can be treated via SPH kernels, and the problem is reduced to minimizing error in the longitudinal direction. In complex flows, however, excess longitudinal dispersion can deplete reactants that are rotated and placed into lateral contact, so depending on the configuration of reactants, longitudinal errors in one location can influence reaction errors in another (see, e.g., de Barros et al. (2012); Engdahl et al. (2014); Le Borgne et al. (2014)).

The various issues with purely Eulerian and mixed Lagrangian/Eulerian methods motivated the development of purely Lagrangian transport and reaction algorithms. The Lagrangian particle-tracking (PT) method for simulating *passive scalar* transport has several features that have justified their continued development and implementation (Bechtold et al., 2011; Labolle et al., 1996; Salamon et al., 2006b). These include (1) independence of the simulation speed from the underlying velocity (and hydraulic conductivity) discretization, (2) computationally simple representation of temporal (Benson and Meerschaert, 2009; Salamon et al., 2006a) and/or spatial nonlocality (Zhang et al., 2006), and (3) the lack of artificial mixing and negative concentrations. The PT method was extended to simulate chemical reactions by calculating the physically-based probability of particle collision and subsequent conditional probability of reaction (Benson and Meerschaert, 2008; Bolster et al., 2016). In this framework, the chemical reactions occur without an explicit calculation of concentrations, thus removing the need for interpolation onto an Eulerian grid or using SPH kernels for dispersion and reaction calculation (e.g. Tompson and Dougherty, 1992; Prommer, 2006; Avesani et al., 2015), which can reintroduce numerical dispersion and other interpolation errors. Instead, the proximity of particles in the flow field dictate the occurrence of reactions. This point highlights a potential advantage of the PT method over Eulerian reactive transport models because imperfect mixing and chemical spatial heterogeneity are represented by particle numbers and proximities at all scales (Paster et al., 2013; 2014), whereas perfect mixing is assumed at some scale in grid-based models. Furthermore, this PT reaction algorithm can be derived and applied to experimental data without the need for empirical parameters such as effective reaction radii or rates, providing a direct link to the physical mechanics of chemical reactions (Ding et al., 2012).

One of the goals of the work on PT methods is to provide a theoretical basis for upscaling effective reaction rates in heterogeneous flow fields within larger-scale Eulerian codes, based on subgrid fluid deformation metrics (de Barros et al., 2012; Engdahl et al., 2014). When an incompressible fluid moves through porous media, the velocity field influences reactions by deforming a hypothetical fluid parcel. Gradients in the velocity field will cause stretching of the fluid parcel in one dimension which is accompanied by compression in others. Compression can bring fluids of different composition into closer proximity, facilitating mixing and immediate (or future) reactions. In 3-D, twisting flow and eddy-like whirls can significantly add to enhanced mixing by fluid deformation (Bakker and Hemker, 2004; Chiogna et al., 2014). Fluid deformation enhances mixing, which cannot be undone (Cirpka et al., 2011; Werth et al., 2006). This mixing is poorly constrained in many grid-based models, leading to incorrect effective reaction rates. The PT reaction theory has been used to estimate the increased reaction rates that may accompany any sort of fluid deformation (Engdahl et al., 2014). This work parallels similar work that examines Eulerian deformation metrics (de Barros et al., 2012; Le Borgne et al., 2014) and the similarities may provide a connection between the Eulerian and Lagrangian methods for simulating deformation-enhanced reactions. In other words, the PT methods provide a computationally simple way to inform larger upscaled grids about the increased reaction rates that are engendered by subgrid fluid deformations.

However, it remains to be shown the conditions under which the PT and Eulerian methods converge to the same solutions for a given boundary value problem (BVP). Because mixing-driven reactions can be highly non-linear, the simulated mass of the products and reactants may be highly sensitive to any transport errors. In this work we construct a few simple problems that isolate (and/or eliminate) potential sources of error to investigate the supposed similarity of the methods used to simulate a basic set of n coupled advection-diffusion-reaction equations (ADRE)

$$\frac{\partial C_i}{\partial t} = -\nabla \cdot (\boldsymbol{\nu} C_i - \boldsymbol{D}\nabla C_i) + R(C_1, C_2, \ldots, C_n); \quad i = 1, \ldots, n, \qquad (1)$$

where C_i is the concentration of species i, $\boldsymbol{\nu}$ is the local mean velocity vector, $\boldsymbol{D}$ is a dispersion tensor, and $R()$ is a reaction function of all n species. We investigate simulation of dispersion using either a constant $D_{ij} = D_m\delta_{ij}$ or a velocity-dependent $D_{ij} = (|\boldsymbol{\nu}|\alpha_T + D_m)\delta_{ij} + (\alpha_L - \alpha_T)\nu_i\nu_j/|\boldsymbol{\nu}|$, where D_m is a diffusion-like constant, $\alpha_L \geq \alpha_T$ are longitudinal and transverse dispersivities, and δ_{ij} is the Kronecker delta. The reaction rate is typically dictated by the law of mass action, and non-equilibrium rates must often be estimated empirically (Apello and Postma, 2005).

In general terms, any grid-based approximation of (1) will incur several types of error. Foremost is the difficulty in representing a sharp interface with points spaced some distance away from each other in the hyperbolic (advection) portion, along with lesser amounts in the parabolic (dispersive) portion. Additional error in the reaction term arises by representing the various (subgrid) concentration values for each species in a cell by single values. Less obvious are errors incurred in the approximation of the velocity vectors (Benson et al., 1998), and error from sequentially solving several components of the equation by operator splitting (Toro, 2009). In any realistic heterogeneous flow field simulation, the various errors will have different magnitudes in different regions of the flow domain because of different velocity magnitudes, orientations relative to a grid, and different concentration, velocity, and dispersion coefficient gradient magnitudes and orientations.

On the other hand, the discrete and potentially stochastic nature of the PT simulations means that simulation of a deterministic BVP can be numerically taxing, as an ensemble of simulations is often needed to ascertain statistics of the solutions. Moreover, the reactions have been shown to depend on the number of particles used: we specify only the positions of particles, so that the initial concentration is approximated by a sum of Dirac delta functions. The initial concentration can only be everywhere equal when the number of particles goes to infinity. Conversely, smaller numbers of particles represent greater heterogeneity in the initial concentration field (in this case, greater correlation length of concentration fluctuations (Paster et al., 2014)). This heterogeneity may increase over the duration of the simulation. Finally, it is currently necessary to solve the transport and reactions sequentially, so that error is incurred in the operator splitting. Therefore, it is unclear if the PT simulations will converge to a "correct" solution for a realistic problem, or if a small number of realizations is sufficiently representative of the ensemble mean.

Our goal is to compare various aspects of Eulerian and PT simulations of (1). To do so we set up a series of simulations with increasing complexity. The first problem considered here is simple 1-*d* flow aligned along an x-axis in a 2-*d* domain. Diffusion is spatially uniform and isotropic. Reaction is limited to a simple (albeit non-linear) irreversible bimolecular system $A + B \rightarrow P$, as this system has been widely used to analyze reactive transport behav-

ior and has been shown to be a fundamental building block of more complex reaction chains (Gillespie, 1977; 2000). The reaction term in Eq. (1) is $R(C_A, C_B) = -k_f C_A C_B$. For ease of visualization, the product P is made immobile. In uniform flow, all of the advection algorithms used here can be made free of error, so we can isolate diffusion/reaction errors. Following this comparison of PT and Eulerian convergence, a more complex heterogeneous velocity field is used to check the magnitude of errors introduced by Eulerian approximations of the heterogeneous advective fluxes.

2. Overview of error in Eulerian solutions

A common approach to solving the ADRE (1) on a grid is to use operator splitting and sequentially solve the advection, diffusion, and reaction terms. The many algorithms (e.g., Sweby, 1984; Leonard, 1991; LeVeque, 2002; Bokanowski and Zidani, 2007) for the hyperbolic advection portion are well-known to produce varying degrees of numerical dispersion and/or oscillation and overshoot due to the truncation of higher-order space and time derivatives in the representation of the variability of the concentration. We investigate the family of TVD models (including the simplest and best known first-difference upwind weighted scheme) with a forward Euler time approximation on uniform space-time grids of $(\Delta x,\ \Delta t)$. We choose these algorithms because for a Courant number defined in any direction i by $\lambda = v_i \Delta t / \Delta x_i$ of unity, the advection term is known to be free of numerical dispersion. The Courant number is a measure of how far solute is allowed to traverse any grid block, and most grid-based solutions require $\lambda \leq 1$. In a heterogeneous flow domain, the Courant number is never uniformly unity, and higher-order algorithms that use Courant-based flux limiters are more accurate; however, numerical error is never eliminated entirely from the solution, and these algorithms require more computation time. The benefit is a reduction in the number of nodes required to get "equivalent" solutions to the lower-order algorithms. As well, many other schemes can be adopted to manage the error and computational cost of Eulerian methods including adaptive refinement of grids where necessary (e.g., (Henshaw and Schwendeman, 2003)) or more accurate timestep interpolation (e.g., (Tambue et al., 2010)). However, there is no consensus on the most appropriate algorithm, and solutions based on 1st-, 2nd-, and 3rd-order accuracy in space on uniform grids are common.

Generally speaking, the discretized diffusion operator is thought to be sufficiently error-free, relative to any advective error. On the other hand, application of the law of mass action for the reaction term assumes perfect mixing within any Eulerian block. The effect of subgrid concentration perturbations are not resolved by the numerical method. Recent studies have focused on this effect and shown that incomplete mixing effects can be strong, leading to significantly altered reaction rates (Benson and Meerschaert, 2008; Chiogna and Bellin, 2013; Paster et al., 2013; 2014; Porta et al., 2016) compared to those predicted by the assumption of perfect mixing. The non-linear nature of the reactions can make the simple act of concentration averaging highly variable (e.g., Battiato and Tartakovsky, 2011; Battiato et al., 2009; Schwede et al., 2008). Newer formulations of the reaction term can account for subgrid concentration variability by assuming both a distribution of concentration and a subgrid mixing rate, but this method requires calibration with measured reactions at the approprtiate scale (e.g., (Chiogna and Bellin, 2013)). In short, the "spikier" the unknown subgrid concentration heterogeneity and the more nonlinear the reaction, the greater the averaging error that will occur.

3. Overview of error in Lagrangian solutions

In the PT simulations at hand, the advection of individual particles can be made essentially free from error by using Pollock's algorithm (Pollock, 1988). For the explicit Euler approximation we use here, the advection error is negligible as long as the velocity field is fairly smooth (Benson et al., 1998). The diffusion operator can be made arbitrarily accurate in the mean by using motions that solve the correct Fokker-Planck equation (Bechtold et al., 2011; Labolle et al., 1996; Salamon et al., 2006b). For example, if a spatially heterogeneous dispersion equation is being solved, then the motions are generated according to an Itô implementation of the nonlinear Langevin equation for Gaussian random walks ((Labolle et al., 1996; Salamon et al., 2006b), and see Appendix C). If post-simulation reconstruction of the concentration field is required, errors arise with variance related to the particle numbers, binning size and smoothing kernels used (e.g., Chakraborty et al., 2009; Pedretti and Fernàndez-Garcia, 2013). A similar problem to the "subgrid" concentration fluctuation is present for PT methods, in that a sufficient number of particles must be used to resolve the small-scale correlation structure of the concentration fields (Ding et al., 2012).

There are several methods for calculating the chemical reactions among the particles. Many are based on an on-off (binary) type of reaction calculation based on the hard-shell particle "radius" model (Doi, 1976; von Smoluchowski, 1917). If two particles are located within this radius, then a reaction takes place (Edery et al., 2009; Hansen et al., 2014). Others are based on a calculation of the probability that two particles will be collocated based on dispersion motion (Benson and Meerschaert, 2008; van Zon and ten Wolde, 2005). This method is readily extended to spatially nonlocal dispersion (e.g., Bolster et al., 2012). The co-location probability is then multiplied by the conditional probability that two co-located particles will react. This latter probability is a simple statement of the thermodynamic reaction rate (Gillespie, 2000; Isaacson, 2013) so the particles are not forced to react (i.e., slow reactions may require multiple co-locations, while fast ones may require very few before a reaction actually occurs). In these models, no lattice is used, so the separations are real-valued and the probability of collision is not binary. This approach can be made arbitrarily accurate without the need for empirical parameters (Paster et al., 2014). Bolster et al. (2016) extend the algorithm by replacing the probability of conversion with a particle mass-fraction loss. Their algorithm gains resolution of low concentrations but has not been rigorously tested for convergence to the original particle birth-death algorithm, so we partially address this issue here. In particular, the original bimolecular algorithm of Benson and Meerschaert (2008) converts entire reactant A and B particles into entire product P particles, so that number of $A + P$ particles remains constant in these simulations. However, the lowest possible resolved concentrations are $\mathcal{O}(1/N_A)$, where N_A is the original number of A particles. (Bolster et al., 2016) convert portions of each particle's mass during a reaction, so that low concentrations are infinitely resolvable, but: (1) numerically, a nearby P particle must be located, or (2) the product mass must be mapped to a fixed grid of concentration, given some binning procedure. Here we choose the latter with product mass mapped to the nearest square grid.

4. Convergence of the diffusion/reaction operations

Because we later investigate the solutions in heterogeneous 2-d velocity fields, we first choose identical 2-d solutions with homogeneous velocity to isolate the diffusion/reaction portion of the ADRE. A series of simulations was constructed using geologically-relevant parameters for transport and interaction of two fluids in a 1000 m × 1000 m aquifer domain. Two fluids are placed next to each other in 15.6 m strips, separated by an initially sharp interface (Fig. 1a). The aquifer has a mean hydraulic conductivity $K = 1$ m/d, a uniform head gradient in the x-direction of 0.01, and a porosity of 0.3. The fluid velocity is uniform at 1/30 m/d aligned

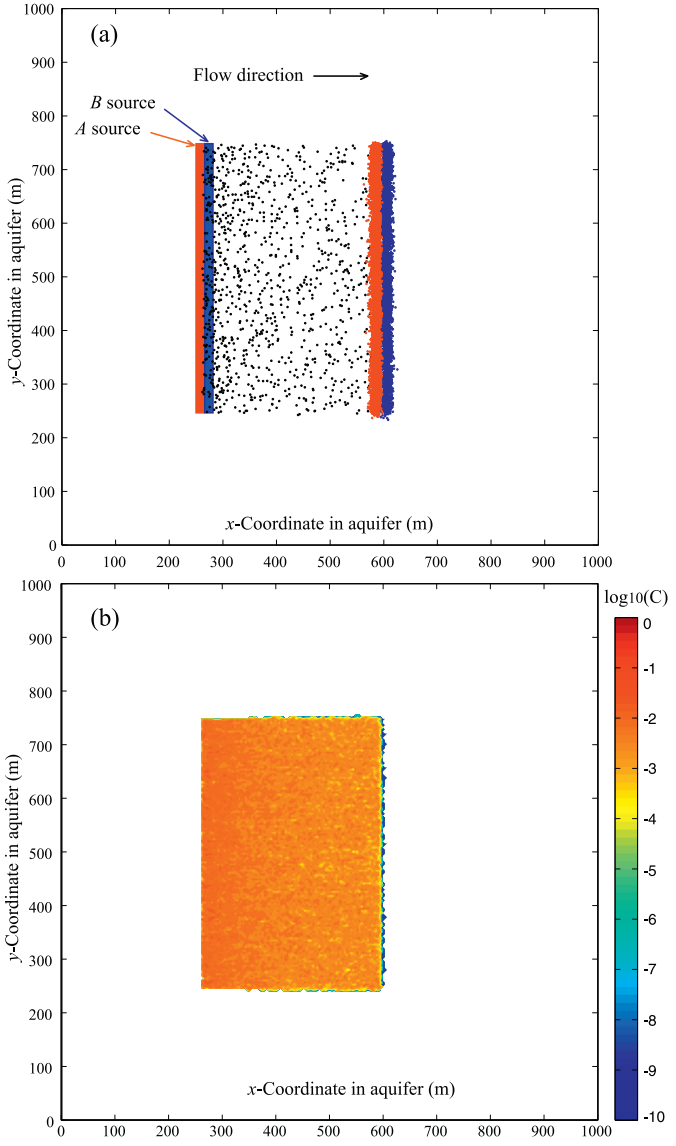

Fig. 1. (a) Aquifer domain showing location of initial reactants A (red rectangle) and B (blue rectangle) for both PT and Eulerian simulations. Also shown are the single-realization locations of individual particles of product P (black) and reactants A (red) and B (blue) for initial particle numbers $N_A(t=0) = N_B(t=0) = 5,000$. (b) Base-10 logarithm of binned product concentrations (colorbar shows $\log_{10}(Molar)$) from an ensemble of 10 particle-number preserving (Bolster et al., 2016) simulations, using bin size of $\Delta x = \Delta y = 4$ m. The colorbar is scaled to match later plots – it does not show all of the low-concentration detail. (For interpretation of the references to colour in this figure legend, the reader is referred to the web version of this article.)

with the x-axis. The dispersion is made uniform and isotropic at 0.001 m^2/d, representing an isotropic local dispersivity of 0.03 m. It is made homogeneous to allow comparisons with 1-d analytic models (Appendix B). The fluids are placed at mean concentrations of 1 M (molar), and the reaction follows the law of mass action $R(C_A, C_B) = -k_f C_A C_B$ with rate coefficient $k_f = 0.01$ (M d)$^{-1}$. We assume unit activity coefficients for simplicity. This rate was chosen so that a significant fraction of the reactants (on the order of 20%) will be consumed after 10,000 days of transport in the simplest case. Approximate measures of the reaction versus transport rates are given by either the advective or diffusive Damköhler numbers $Da_v = k_f C_0/(\boldsymbol{v}/L)$ and $Da_D = k_f C_0/(D/L^2)$, where L is a characteristic scale of transport. For local-scale Da, we choose $L \approx 1$m, so for the uniform velocity case, we have $Da_v \approx 0.3$ and $Da_D \approx 10$. Neither of these numbers point to particularly slow or fast reactions relative to transport.

To compare the grid-based and PT codes, we should choose similar initial conditions (ICs). It has been shown that the PT codes inherently represent spatial variability in the initial condition and also as the particles diffuse and react: the spatial autocovariance decreases with increased particle number. Paster et al. (2014) show that, for the Dirac-delta function particles that we use here, the initial particle number N_0 is related to the auto-covariance structure of the initial concentrations by $N_0 = C_0^2 A_{strip}/(\sigma_C^2 I^d)$, where A_{strip} is the area over which the particles are placed, and $\sigma_C^2 I^d$ is the d-dimensional integral of the covariance function (i.e., the concentration variance times the d-dimensional correlation length). The concentration IC becomes smoother as the number of particles gets larger. Therefore, for the grid-based codes we choose initial concentrations that are deterministically uniform. We also uniformly and randomly distribute the particles in the same size strips as in the Eulerian codes (Fig. 1) and vary the number of particles.

4.1. L^1 convergence

The Eulerian code was run at different discretizations while holding the Courant number $\lambda = 1$. The first check of convergence is the integrated mass of product after 10,000 days (i.e., the spatial L^1 convergence). The Eulerian solutions appear to converge in this sense at $\Delta x \leq 1$ m and a total reaction completion of 22.08% (Fig. 2). Because of the 2-d nature of the problem and a low-to-intermediate value of $Da_v \approx 0.3$, we only have an approximate analytic solution to this problem (B.1), so the check of convergence is relative stability of the solution at 22.08%.

Because the initial particle locations and the dispersion motions both have random components, the PT simulations are stochastic in nature: each solution will give slightly different results. Here we show the mean and standard deviations of the integrated mass of product for an ensemble of 20 particle-killing simulations (Fig. 2). The non-deterministic nature implies that the initial conditions have some inherent randomness that should be constructed to represent the actual physical heterogeneity (Ding et al., 2012). The number of particles encodes the spatial autocorrelation of initial concentrations, and simulations with different number of initial particles are supposed to give different results. Therefore, our check of convergence follows two tacks: varying the number of particles and the time-step size. As the former becomes larger, the effective concentration correlation length becomes a smaller fraction of the size of the specified initial condition structure (i.e., a better-mixed I.C.) and should mimic the homogeneous deterministic initial condition and solution given by the Eulerian simulations. Indeed, increasing the number of particles shows this kind of convergence to a reaction completion of 22.10% in the particle-killing simulations (Fig. 2). The inter-simulation variability also decreases when the particle density increases, as expected. It appears that the converged Eulerian (with $\Delta x = 0.98$ m) and Lagrangian solutions are very similar when the initial number of A and B particles is 20,000 (22.05% and 21.94%, respectively).

We also checked the solutions when the timestep size was varied, and also checked the newer algorithm (Bolster et al., 2016) that does not kill reactant particles (instead, the particle masses are allowed to decrease). These simulations are more accurate at lower concentrations with the tradeoff of longer simulation times. We checked the simulations for initial particle numbers of 10,000 at different Δt over a very large range. The means of the particle-killing and particle-preserving algorithms are not statistically significantly different at the particle number and timestep resolutions duplicated here (Fig. 2 inset).

As explained by Paster et al. (2014) (and reiterated by Hansen et al. (2014)), there is a potential for multiple particle collisions during a single timestep that may be under-estimated by large Δt. The neglect of the diminishing survival probability should tend to

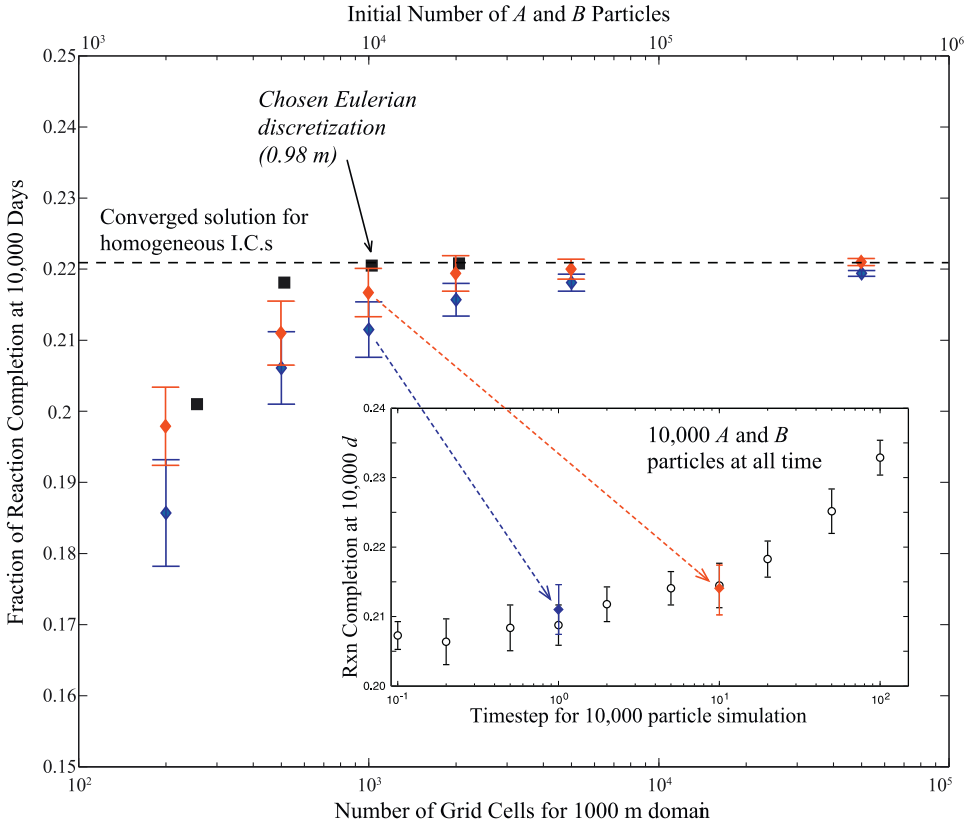

Fig. 2. Degree of reaction completion within Eulerian (solid squares) and PT simulations (whiskers denoting $\pm 1\sigma$). Red and blue denote $\Delta t = 10$ and 1 d, respectively. The top x-axis represents initial number of both A and B particles; the bottom x-axis is the number of finite-difference grids for 1,000 m domain (i.e., $\Delta x = 1,000/N_g$ m). All solutions appear to converge to a reaction completion of 22.1%. Based on similarity, convergence, and speed of solution, the "base-cases" of 40,000 particles and 1024 finite-difference grids (both highlighted) are chosen. (For interpretation of the references to colour in this figure legend, the reader is referred to the web version of this article.)

over-estimate reactions for too large a Δt. On the other hand, too small a timestep reduces the area "probed" by a particle and reduces the number of potential reaction partners, until, as $\Delta t \rightarrow 0$, only the nearest neighbors are allowed to react. So too small a timestep should tend to underestimate reaction rates. The correct Δt lies between a lower value dictated by the average particle density and an upper number dictated by several stability criteria. We may bracket the timestep size by the ratio of the effective search radius for a particle pair undergoing diffusion to average particle spacing $0.25 < 2\sqrt{8D_m\Delta t}/\Delta x < 1.5$ (Paster et al., 2014). The factor 8 in the square root differs from pure diffusion and comes from the convolution of two Gaussians representing the co-location probability (Appendix C). The initial condition area A_{strip} over the particle number of one species $N_A(t)$ gives a first-order approximation of inter-particle spacing. In the simulations at hand, $D_m = 0.001m^2/d$, and average inter-particle distance $A_{strip}/N_A(t = 0) \approx 0.78m$, so $1.2\,d < \Delta t < 340d$. Varying the timestep over a wide range shows that the solutions have an inflection point between too little and too much reaction at the point surrounding the smaller of the two values (Fig. 2 inset). From approximately $\Delta t \leq 10$, the mean product concentrations are not significantly different, so in general we recommend setting $\Delta t < 0.16\Delta x^2/D_m$.

4.2. Pointwise (L^∞) convergence

Because the Eulerian simulations are deterministic, we may also look at the shapes of the product distributions to assess qualitatively the pointwise convergence (Fig. 3). The peak concentrations in the 1st-order upwind simulations continue to rise significantly over the range of discretizations tested (the finest discretization model comprised over 4 million cells), so that pointwise convergence was not seen in these simulations. Similar, but lower magnitude, issues were seen in simulations using 2nd- and 3rd-order TVD simulations (Appendix A). If maximum concentrations are a concern to the user, a finer discretization will be required than one derived (later in this paper) for accuracy in the L^1 norm.

In the PT simulations, the concentrations are only created by binning the particles, hence the concentrations will be functions of bin size and any kernels used to model the spatial influence of particles (see, e.g., Fig. 1b). In an effort to compare to the Eulerian results, the mean concentrations along the centerline of the product plume for ensembles of simulations are compared (Fig. 4). The concentrations are simple sums of particle masses in square cells of size $\Delta x = 4$ m. A similar effect in the PT relative to the Eulerian simulations is found when the number of initial particles increases: more particles tend to resolve higher peak mean concentrations. The effect is not enhanced a great deal by the choice of bin size; however, bigger bins will tend to smooth out the higher peak concentrations (Fig. 4). Furthermore, those PT simulations that have total masses of product similar to the Eulerian simulations (for example, 20,000 particles corresponding to $\Delta x = 0.98$ m) also have similar mean peak concentrations. It should be noted that there is considerable variability in the binned product concentrations from the particle-killing algorithm along the plume direction. For example, at the peak location in the 50,000 particle, 256 bin simulation, the product concentrations had a standard deviation of approximately 0.0065 M (compared to the mean concentration of 0.037 M).

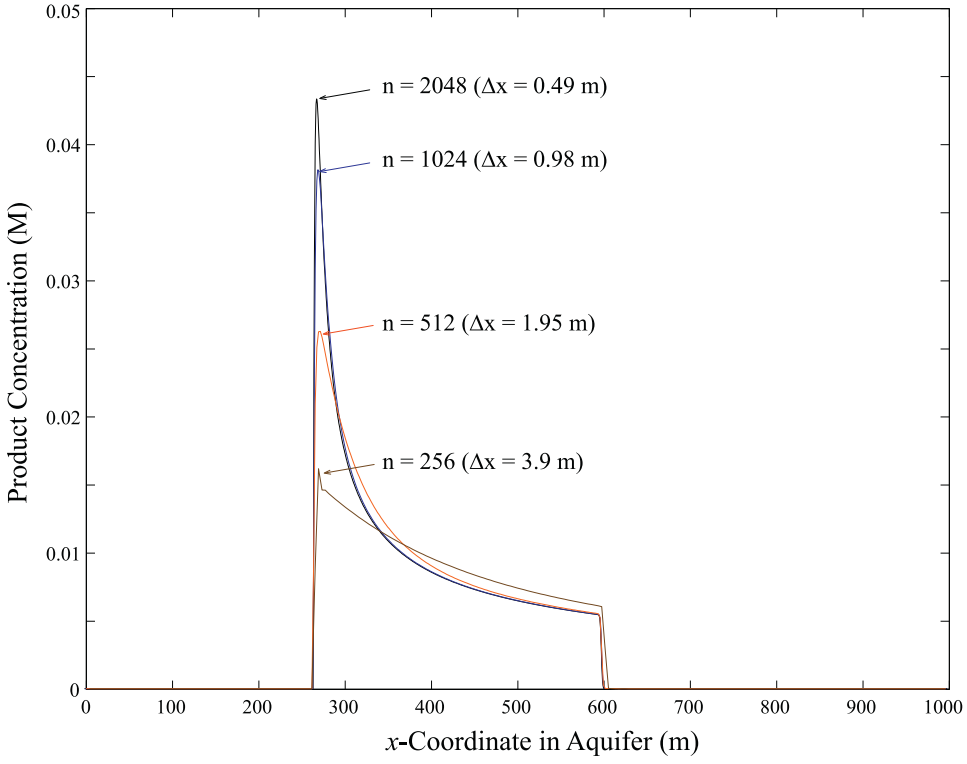

Fig. 3. Product concentrations along horizontal slices of the aquifer for all upstream Eulerian schemes (because all have zero numerical dispersion for Courant number $\lambda = 1$) using different discretizations. Any deviations are due to different mixing at different discretizations.

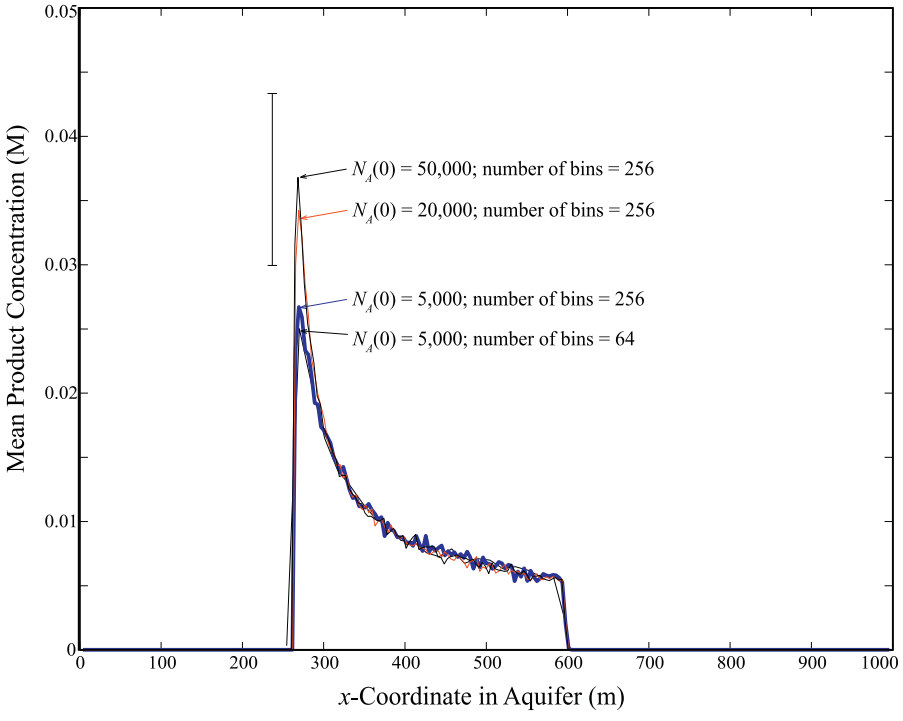

Fig. 4. Averaged product concentrations from particle-killing PT simulations along horizontal slices of the aquifer using different number of initial particles $N_A(0)$ and bin sizes (indicated by number of bins in x-direction). The vertical whisker bar denotes $\pm 1\sigma$ for the 50,000 particle peak concentration.

5. Eulerian velocity error

The spatial approximation using 1st-order upwind advection scheme used here has a known numerical dispersion of magnitude $\frac{|v|\Delta x}{2}(1-\lambda)$ (LeVeque, 1992). A similar magnitude error is incurred by the forward Euler time-stepping, so the total error is of order $|v|\Delta x(1-\lambda)$. Here we investigate (1) the combined effect of changing both Δx and λ in a simple homogeneous velocity field and (2) the effect of spatially variable λ in a more realistic heterogeneous field. We also implement a 3rd-order TVD and the particle-number-preserving Lagrangian algorithms on the same velocity fields.

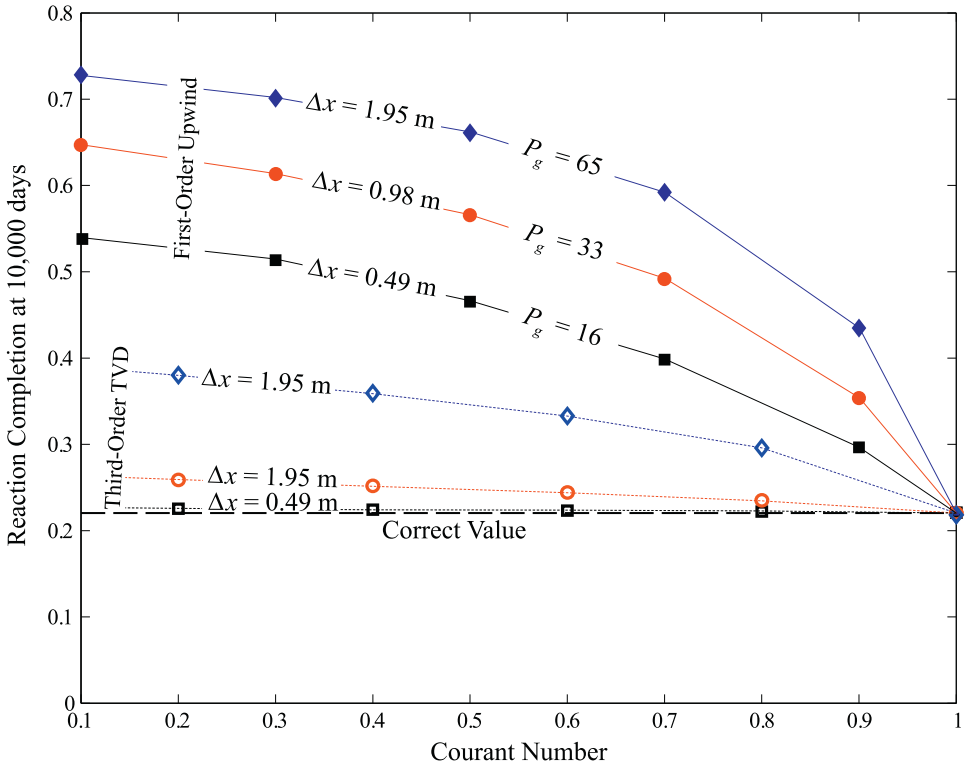

Fig. 5. Amount of product produced in Eulerian simulations at 10,000 days by the 1st-order upwind (filled symbols) and 3rd-order TVD schemes (open symbols) with different space and time discretizations. Lines added to aid visualization.

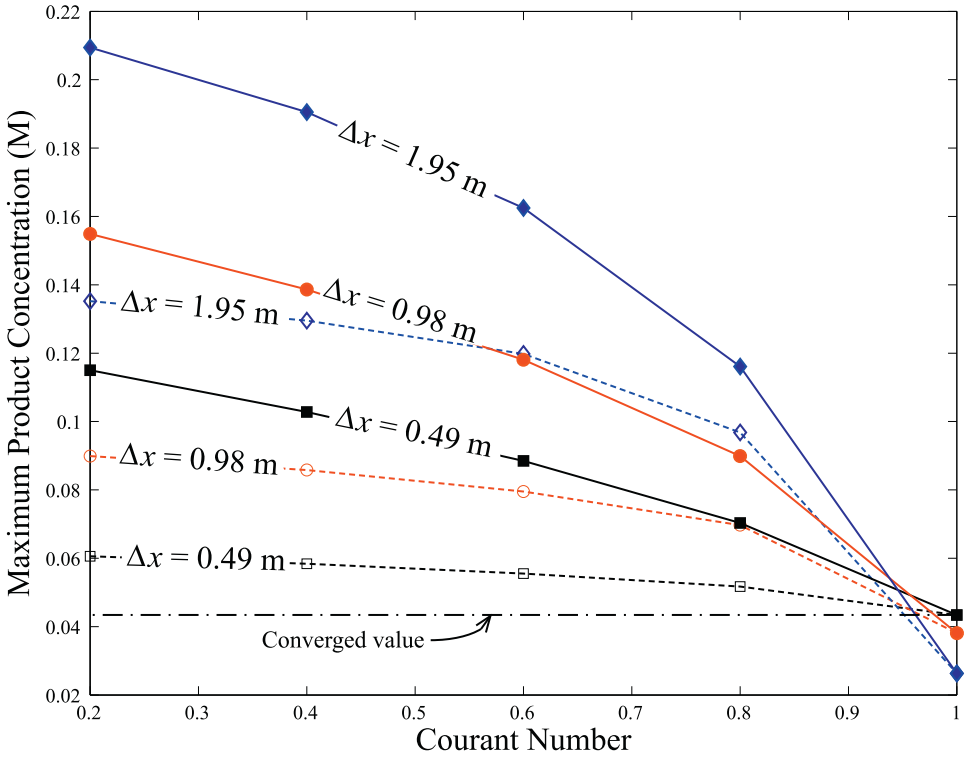

Fig. 6. Maximum product concentration in Eulerian simulations at 10,000 days by the 1st-order upwind (filled symbols, solid connecting lines) and 3rd-order TVD schemes (open symbols, dashed connecting lines) with different space and time discretizations. Lines added to aid visualization.

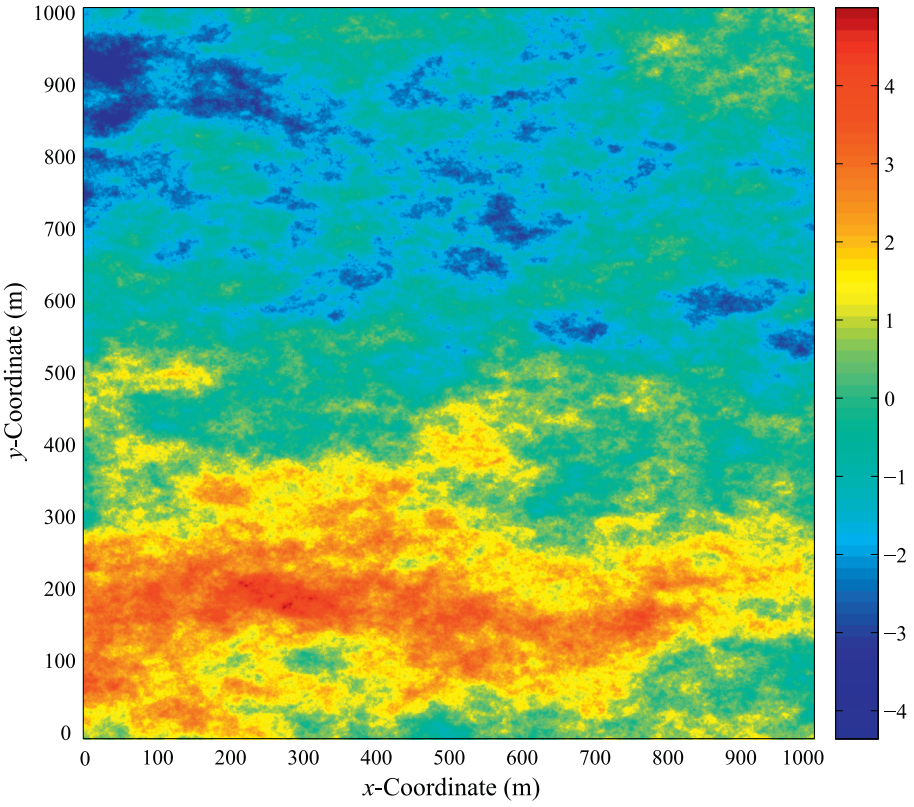

Fig. 7. Anisotropic, or matrix-scaling fractional Brownian motion K field. Color bar represents values of $\ln(K)$ in m/d.

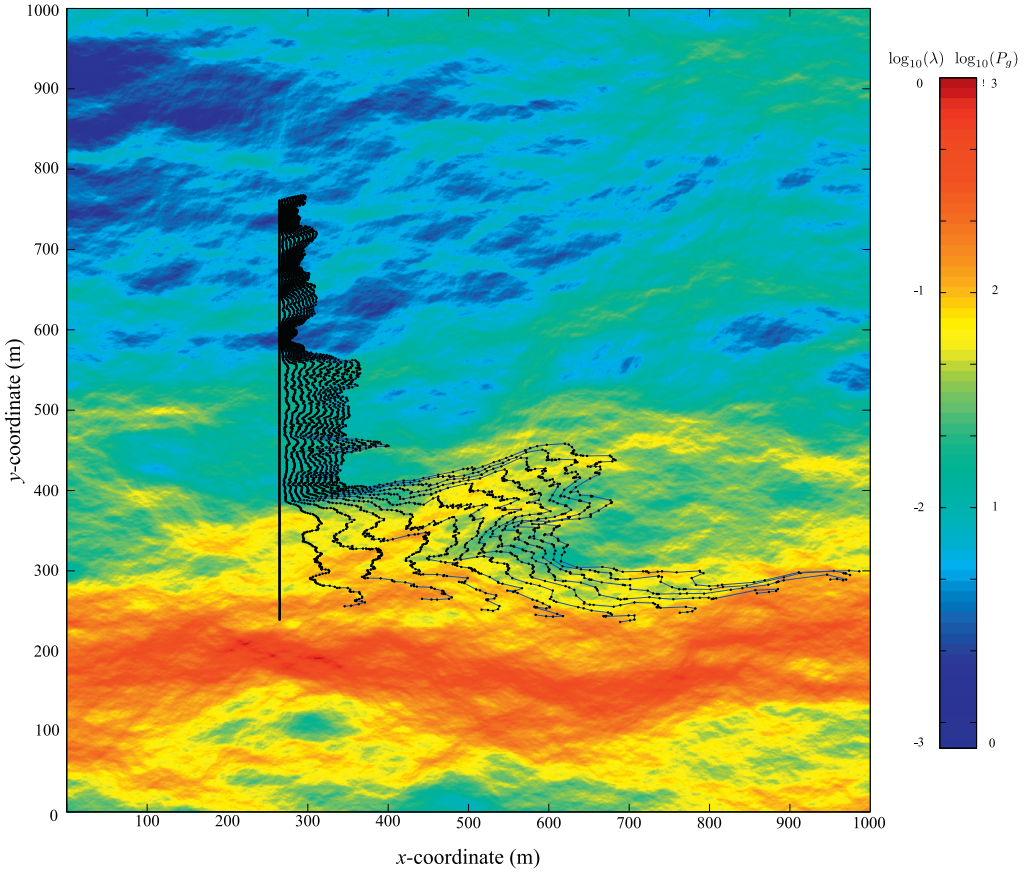

Fig. 8. Pure advection of a line of 500 particles (black dots) initially placed at the location of reactant interface $x = 256$ m. The blue line connects initially adjacent particles that were placed 1 m apart. The background colors are the logarithm of velocity magnitudes, with higher velocities represented by warmer colors. The colorbar shows the velocities converted to Courant (λ) and grid Peclet (P_g) numbers. Highlighted areas show regions of shear, compression, and dilation relative to local flow direction. (For interpretation of the references to colour in this figure legend, the reader is referred to the web version of this article.)

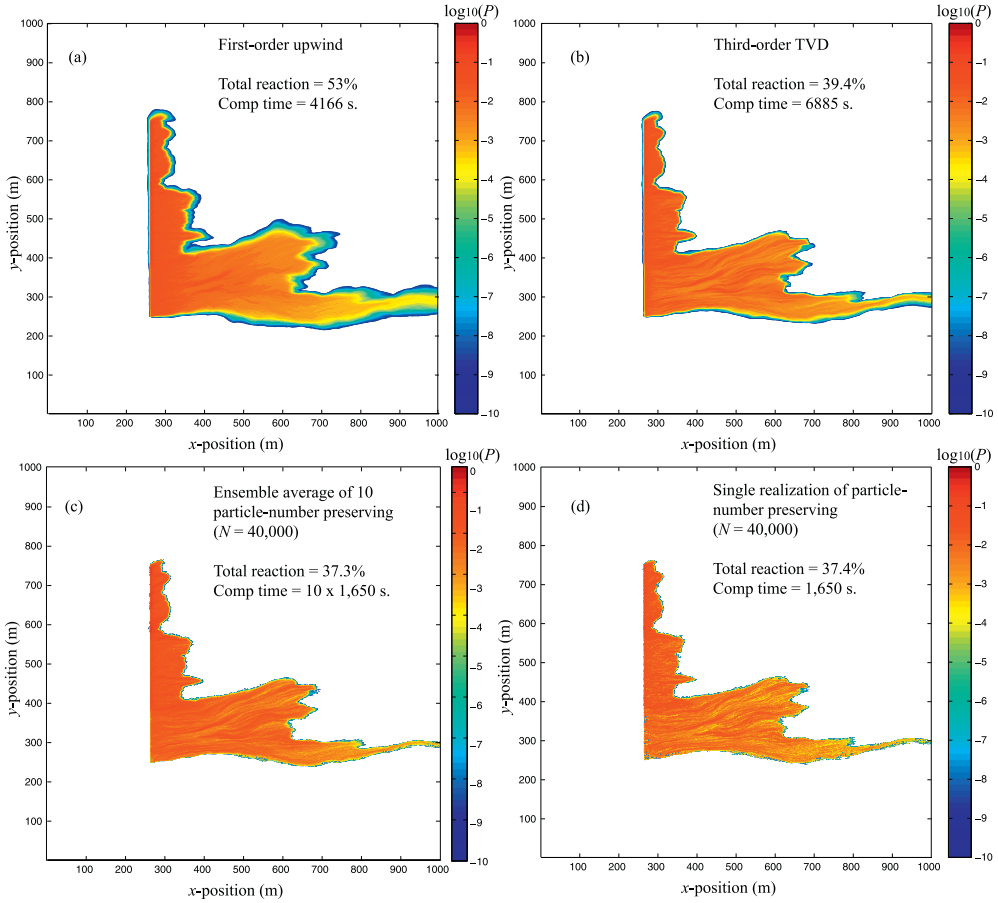

Fig. 9. Base-10 logarithms of simulated product concentrations at 10,000 days using constant $D = 0.001m^2/d$: (a) (Eulerian) first-order upwind, (b) (Eulerian) third-order TVD, (c) Ensemble average of particle-preserving PT, and (d) Single realization from (c). Colorbars denotes Molar product concentration. TVD simulations have large areas of negative concentrations, so plots only show concentrations above 10^{-20} M.

5.1. Homogeneous velocity

For the homogeneous velocity case, the Courant number λ was varied between 0.1 and unity for three levels of discretization (Δx = 0.49, 0.98, and 1.95). The reacted masses at 10,000 days increased, in some cases dramatically, at all $\lambda < 1$ (Fig. 5) due to spurious numerical dispersion and erroneous mixing, particularly in the 1st-order upwind algorithm. The amount of product doubled or tripled at the lowest Courant numbers and highest Peclet numbers. In Appendix B we demonstrate semi-analytically how changes in dispersion coefficient might affect the total mass of product produced. The total mass of product produced, for either fast or slow bimolecular reactions, scales approximately as $\sqrt{D}$, meaning that any errors in D, arising from numerical dispersion, can result in significantly larger masses of product. For 1st-order, explicit forward Euler solutions, the numerical dispersion has a maximum on the order $|v|\Delta x$ so the grid Peclet number ($P_g = v_{\max}\Delta x/D$) is a measure of the ratio of spurious to real dispersion. For velocity-dependent dispersion this reduces to $P_g \approx \Delta x/\alpha_L$. A value of $P_g = 2$ means that real and spurious dispersion are of the same order, and excess product on the order of $\sqrt{2}$ times the correct amount is produced. In general, the maximum amount of error is approximately $\sqrt{1 + P_g/2} - 1$, so that obtaining 5% mass error from a 1st-order accurate algorithm would require $P_g \approx 0.2$.

The 3rd-order TVD scheme appears to give reasonable reaction totals (in the integrated L^1 sense) over a large range of λ for $\Delta x \leq 0.5m$, which corresponds to a classical $\Delta x/\alpha_L \leq 16$. Note that for the particle tracking schemes the results with advection are identical to those without advection presented in the previous section due to the principle of Galilean invariance (i.e., a uniform advection merely shifts all particle locations, but does not change their relative distance from one another, which is all that is required for reaction).

The peak concentrations in these Eulerian simulations were also tracked, and at all discretizations there were substantial errors introduced by the advection approximations (Fig. 6). Although not shown here, the 3rd-order advection algorithm converged to less than 5% error in this L^∞ sense at about $\Delta x = 0.1m$, while at this smallest discretization (representing $P_g = 4$) the 1st-order had peak concentrations approximately 50% too high. Also noticeable in these plots is the error due to the diffusion and reaction operators at a Courant number of unity. These numbers correspond to the different peak concentrations shown in Fig. 3.

5.2. Spatially variable velocity

A random fractal K field with anisotropic-, or operator-scaling, was generated using Fourier filter methods (Benson et al., 2013). Operator-scaling in this context means that transects of the K field are fractional Brownian motions with different Hurst coefficients in the x- and y-directions of 0.44 and 0.36 (with uniform weighting on the axes) so that there is greater correlation of the underlying Gaussian increments in the x-direction (Fig. 7). The geometric mean K is 1 m/d to match the uniform velocity field in the previous section. The porosity is set to 0.3 and the mean hydraulic gradient to 0.01. The K and steady-state velocity fields were calculated using a block-centered scheme at a uniform discretization

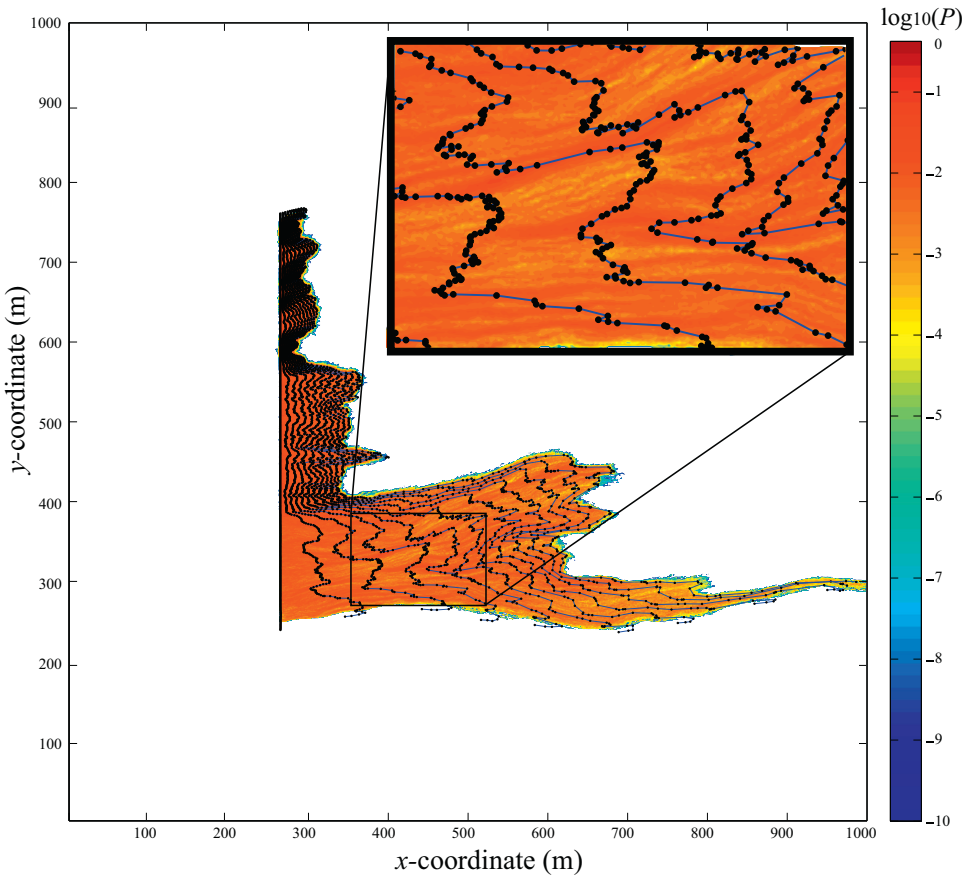

Fig. 10. Overlay of advection-only particle traces (Fig. 8) above base-10 logarithms of simulated product concentrations at 10,000 days from an ensemble average of particle-preserving PT (reproduced from Fig. 9d). Higher reaction rates are consistently found in places where the fluid deformation shows folding and compression lateral to mean flow. Colorbars denotes Molar product concentration.

of $\Delta x = \Delta y = 0.98$ m. To illustrate the general features of the velocity field, a line of uniformly-spaced inert particles was placed along a transect at the initial A/B reactant interface at $x = 256$ m (Fig. 8) and tracked at 1000-day intervals (with a blue line joining initially adjacent particles). The lines and particles allow a rough estimation of the local components of fluid deformation, including shear and dilation/compression transverse to the mean flow direction. Because of the divergence-free (incompressible) flow, any dilation in the flow direction must be accompanied by compression in the orthogonal direction and vice-versa (de Barros et al., 2012; Engdahl et al., 2014).

5.2.1. Isotropic, spatially constant dispersion

Fluid deformation, including shear, can put reactants into closer proximity and increase reaction rates (Engdahl et al., 2014), as verified visually by the locations of generated product particles (mapped to $\log_{10}$(concentration) on a grid of 0.98 × 0.98 m cells) in a 40,000-particle simulation (Fig. 9d). The regions of high deformation, as indicated by stretching and/or shearing flowlines, are expected to be regions of extremely high or hyper-mixing (de Barros et al., 2012; Bolster et al., 2011a). Indeed they tend to be heavily populated with product particles (Fig. 9d). The total amount of product, i.e., the completion of the reaction after 10,000 days, is 37.4% in this simulation, or roughly 70% greater than the total amount of product (22.1%) in the homogeneous domain, all other factors being equal. This increase is due entirely to fluid deformation. An ensemble mean of 10 simulations shows the same features (Fig. 9c), demonstrating that the strong zonation of reaction intensity is not an artifact of random variations between realizations (Fig. 10).

The 3rd-order TVD solutions have unphysical negative concentrations spread throughout the lower-concentration regions, so only concentrations greater than 10^{-20} are shown here. A 1st-order Eulerian simulation with the same velocity field and parameters with $\Delta x = \Delta y = 0.98$ m (or a domain of 1024 × 1024 ≈ 10^6 nodes) gives a total amount of product of 53%, or roughly double the increase seen in the PT simulations going from homogeneous to the heterogeneous velocity fields (Fig. 9a). This overestimation is consistent with the overestimations by the Eulerian simulators in a homogeneous domain for smaller Courant numbers (Fig. 5). Calculated velocities in the heterogeneous domain spanned over three orders-of-magnitude; therefore, the local Courant numbers go from essentially zero to unity across the entire domain (Fig. 8). The numerical dispersion in both the longitudinal and transverse directions (because flow is seldom exactly parallel to the x-axis in the heterogeneous flow field) leads to substantial overestimation of the spatial extent of reaction in both high and low velocity zones (Fig. 9a). The 1st-order Eulerian method does not resolve the fine "threading" of reaction that takes place in areas of high fluid deformation.

The 3rd-order TVD method is visually better at restricting spurious lateral dispersion and preserving structure within the plume (Fig. 9b), and has an integrated product concentration closer to the PT simulations (at 39.4%). For this algorithm, another level of grid refinement (at a cost of 8 times the computation time, addressed in a subsequent section) would be necessary for the simulation to adequately match the PT results. For the first-order algorithm, the

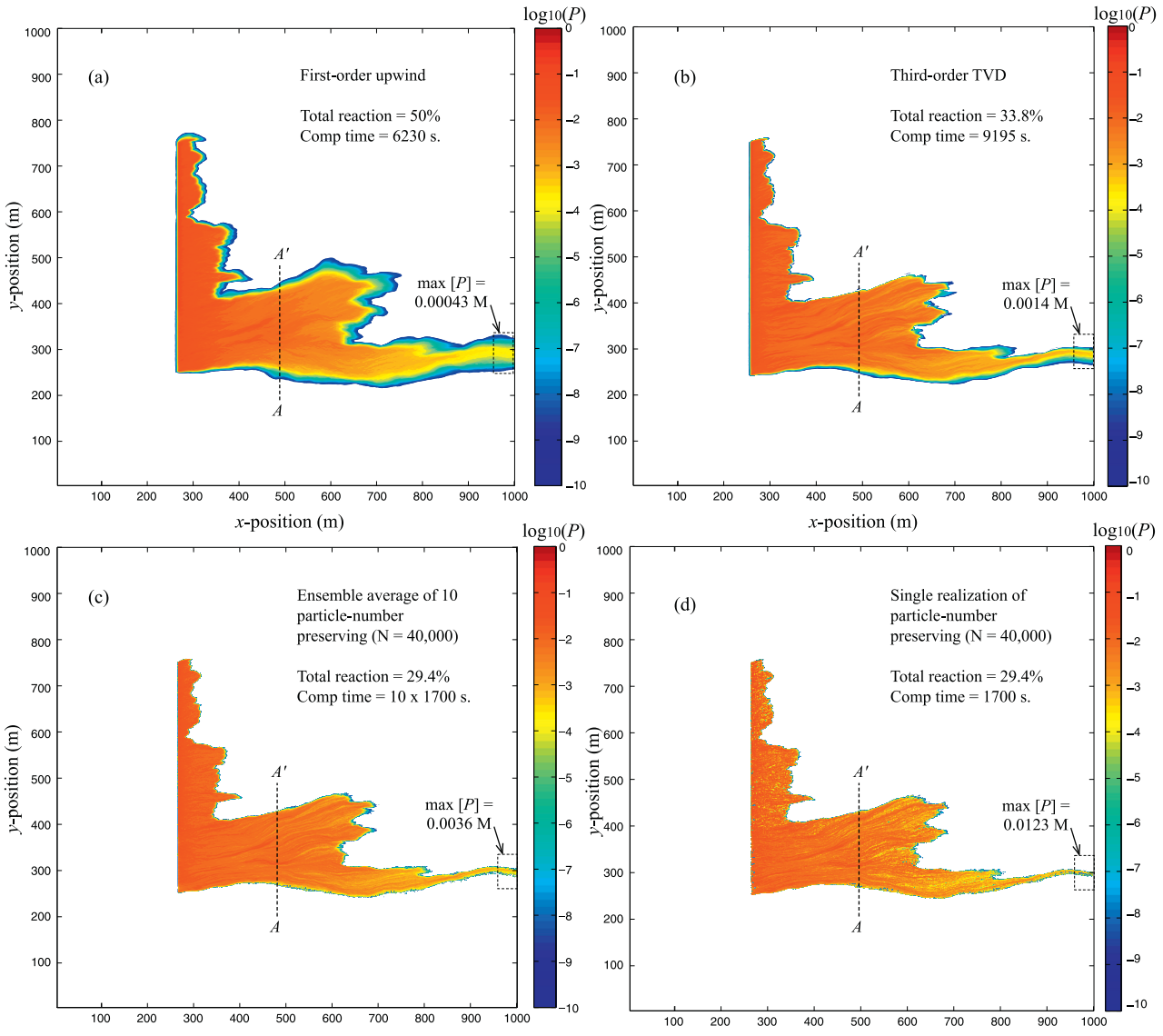

Fig. 11. Base-10 logarithms of simulated product concentrations at 10,000 days using velocity-dependent D with $\alpha_L = 0.1m$: (a) (Eulerian) first-order upwind, (b) (Eulerian) third-order TVD, (c) Ensemble average of particle-preserving PT, and (d) Single realization from (c). Colorbars denotes Molar product concentration. TVD simulation has negative concentrations, so plots only show concentrations above 10^{-20} M.

values of Δx and Δt would need to be reduced to bring the grid Peclet numbers substantially below unity to reduce numerical mixing to less than the real mixing (see Appendix B). In the example used here, on the order of 1 to 100 billion cells would be required, which is far outside the computational resources available to us.

5.2.2. Anisotropic, velocity-dependent dispersion

All of the transport and reaction algorithms are straightforward to extend to velocity-dependent and anisotropic dispersion (Appendix C, (Salamon et al., 2006b; Zheng and Wang, 1999)). The dispersion coefficient (and local dispersivity) at this scale represent subgrid velocities that are not resolved and are a function of flow field variability. Because we are not following the assumptions of low velocity variability and finite and fixed correlation lengths, there are no analytic expressions for effective block dispersivity (de Barros and Dentz, 2016). Instead we use a common assumption that sub-grid dispersion is some fraction of the size of the block (the size at which velocity is resolved). Here we chose $\alpha_L = 0.1\Delta x$, where Δx was held at 0.98 m based on the resolution of the velocities. The transverse dispersivity is set to one-tenth the longitudinal. The timestep size was chosen to maintain $\lambda = 1$ at the highest velocity (which is constant for the Eulerian simulations but may change based on the highest velocity experienced at any time by the particles).

Due to the lower values of dispersion in low-velocity areas (compared to the previous example with $\boldsymbol{D} = 0.001\frac{m^2}{d}\boldsymbol{I}$), the particle-number-preserving PT simulations have lower integrated reaction product of 29.4% relative to the 37.4% in the isotropic $\boldsymbol{D}$ case (Fig. 11c and d).

For the 1st-order upwind simulations, the common block-size based dispersivity choice gives $P_g = 10$. This simulation is very similar, both visually and quantitatively, to the previous isotropic $\boldsymbol{D}$ simulation (compare Figs. 9a and 11a). Each 1st-order simulation indicates reaction completion at about 50% – neither can resolve the subtle differences in the formulation of dispersion. The mixing is dominated by error. The 3rd-order simulation over-estimates

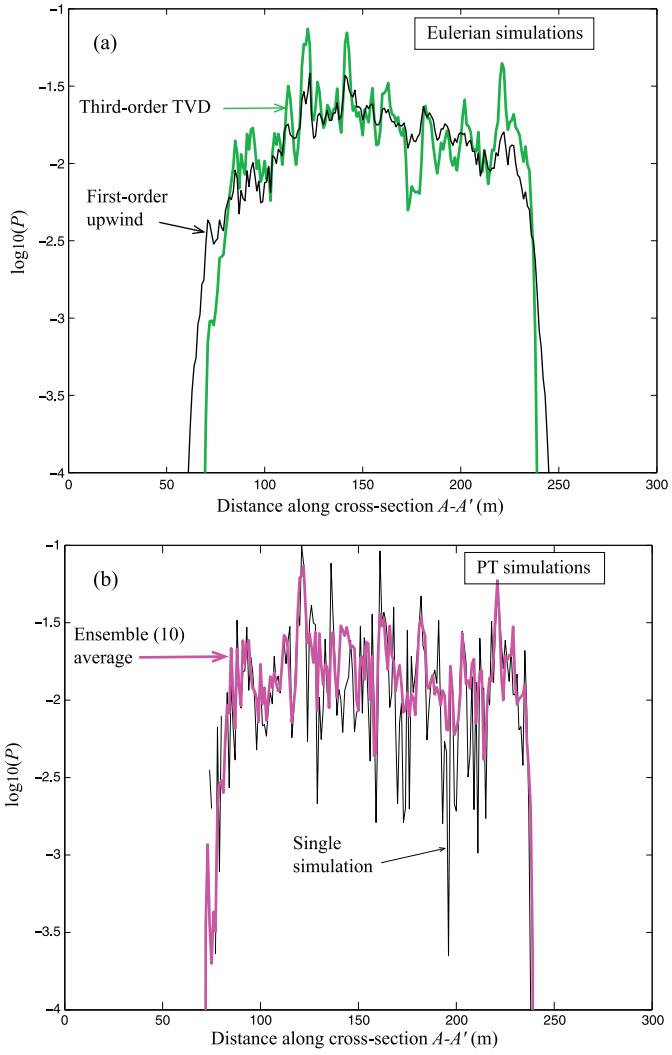

Fig. 12. Vertical cross sections A–A' (see Fig. 11) of product concentrations: (a) Eulerian simulations, and (b) PT simulations—single and ensemble mean of 10 realizations, each with 40,000 particles.

the reactions by several percent (at 33.8%), consistent with the isotropic dispersion and homogeneous velocity cases. However, for both Eulerian simulations, spurious over-mixing in the source area, combined with excess transverse dispersion, depletes the reactants far downstream so that the peak concentrations modeled at the exit area of the aquifer are roughly 3 to 10 times lower than in the PT simulations (compare exit zones in Fig. 11a–d).

A clear feature of the more accurate PT and 3rd-order simulations is the high degree of variability and structure of the product distribution in space (Fig. 11b–d). There is more structure in this simulation than the isotropic $\boldsymbol{D}$ case because of the lower values of transverse dispersion, which limits mixing where the reactant interface has been sheared or folded. A comparison of cross-sections of the product concentrations in the middle of the plume (Fig. 12a and b) shows that the ensemble mean PT and 3rd-order simulations are in agreement, but that a single realization, which represents a potential pathway of an initially heterogeneous plume, has substantially greater variability. Even at a mean transport distance of $\approx$ 250, some product concentrations are 100 times different within $\approx$ 5 m of each other. The peaks and valleys are co-located in the single realization and ensemble plumes, but the combination of fluid deformation and perturbed concentrations in the initial conditions are amplified by the nonlinear reaction. The first-order Eulerian simulation is a poor indicator of reaction heterogeneity.

5.3. Computation time

For a consistent means of comparing computation times, all of the codes were implemented in Matlab on a laptop machine with a 2.7 GHz Intel Core i7 processor and 8GB of 1333 MHz DDR3 RAM (and OSX 10.9.5 operating system). As long as there is enough RAM space, a table of execution times (Fig. 1) verifies that the Eulerian codes require a minimum time $T \approx K_1 \Delta x^{d+1} + K_2$, where T is execution time [s], d is the number of dimensions ($d = 2$ here), K_1 is a constant that depends on the number of executions per node, and K_2 [s] is a small overhead term that accounts for one-time processes such as initialization of arrays. For the homogeneous velocity case, the maximum Courant number of unity forces a minimum execution time with $K_1 \approx 175$ and 285 for 1st- and 3rd-order algorithms. The latter takes about 60% longer to run, all things held constant. The PT simulations are somewhat harder to quantify in the homogeneous velocity case, because there is no Courant number stability restriction. The particle-killing algorithm is more efficient in general, and for a range of values of Δt, it is clear that the computation time increases linearly with $1/\Delta t$ (Fig. 13). The particle-killing algortithm also scales approximately linearly with the initial number of particles (N), while the particle-number-preserving algorithm scales about linearly with small N but appears to scale with the (constant-in-time) number of particles to the 1.2 to 1.6th power for larger numbers (Fig. 13). This is due to the larger number of particles within some constant search radius given as a multiple of $\sqrt{8D\Delta t}$. For the same reason, for large particle numbers, decreasing Δt does not cause a linear slowdown of the particle-preserving method (see the converging computation times for $\Delta t = 50$ and 10 s in Fig. 13). In other words, because the search becomes more efficient when the search radius decreases, the cost is lessened when the timestep is made smaller. Comparing the PT methods to Eulerian, it is clear that single realizations of either PT method takes less time than the stable Eulerian methods. Also, achieving better results in the Eulerian methods by grid refinement is much more taxing than adding particles or changing timestep size in the PT methods.

In the heterogeneous velocity fields, the Eulerian methods still scale with $T \propto \Delta x^3$ in 2-d, but there is an additional penalty of about 20 $\times$ due to the higher maximum velocity in the field. The PT methods also run slower in the heterogeneous fields, but the penalty is only about 1.3 $\times$ to 5 $\times$ because the Courant number of unity applies to the fastest particle, not the fastest velocity anywhere in the domain. Because the velocity distribution is highly skewed (Fig. B.3), the maximum particle velocity is far less than the maximum domain velocity most of the time. Additionally, the number of particles is a modeler's choice dictated by the heterogeneity of the initial conditions. Similarly, the choice of Δt is not as restrictive as in the grid-based methods, so that simulation times for the PT method can be reduced without causing numerically unstable conditions (unlike the Courant requirement of the Eulerian models). In theory, *Pollock's* method can be used analytically in steady flow and semi-analytically in transient flow to determine a particle's advected position over any time interval (Maier and Bürger, 2013; Pollock, 1988), so the chosen timestep is limited by the diffusion and reaction steps.

The reaction step also leads to a particle number stability constraint that arises when dispersion is small: For the particle-number preserving method, the relative change of a particle's mass when reacting with another particle is maximized when two particles (subscripts 1 and 2) are coincident, and then in 2-d, $dm_1/m_1 = k_f m_2/(4\pi\sqrt{det(\boldsymbol{D})})$ (see (Bolster et al., 2016)). The values dm_1/m_1 should be less than unity, so this can be checked at the start of a

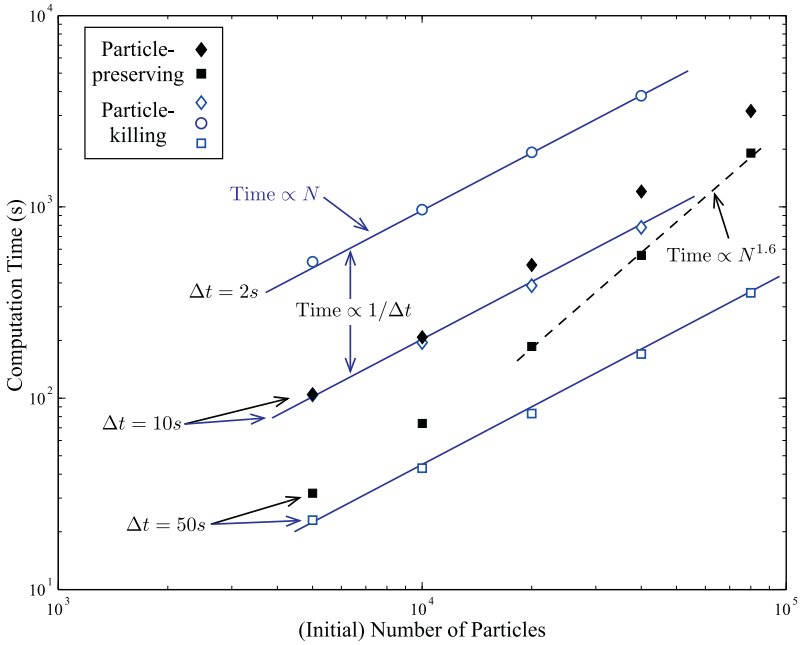

Fig. 13. Execution times for PT simulations for different particle numbers and timestep sizes (symbols) and best-fit lines. Particle-killing simulations (open symbols) scale linearly with initial particle numbers; Particle-preserving algorithm scales with $N^{1.7}$. Both scale with $1/\Delta t$.

Table 1
Execution times (seconds) for Eulerian and PT simulations using uniform, isotropic and heterogeneous, anisotropic dispersion. All Eulerian simulations and PT simulations in heterogeneous velocity use a maximum Courant number of unity. Shaded rows highlight approximately similar solutions in the $\lambda = 1$ homogeneous velocity case.

Homogeneous velocity, $\boldsymbol{D} = 0.001\boldsymbol{I}$							
Eulerian				Lagrangian (per realization)			
Δx	Δt	*1st-order upwind*	*3rd-order TVD*	N	Δt	*Particle-killing*	*Particle-preserving*
0.49	15	1500	2390	40,000	50	170	560
0.98	**30**	**190**	**332**	**20000**	**50**	**83**	**187**
1.96	60	27	48	10,000	50	43	74
				5000	50	23	32
				40,000	10	780	1207
				20,000	10	387	498
				10,000	10	195	209
				5000	10	104	105
Heterogeneous velocity, $\alpha_L = 0.098m; \alpha_T = 0.0098m$							
0.98	1.33	4106	6669	40,000	varies	935	1650
				20,000	O(5–10)	472	684
				10,000		245	320
				5000		140	173

simulation when m_2 is largest, and $\det(\boldsymbol{D})$ is checked at its smallest location. Then the number of particles is increased until m_2 is a small enough number.

6. Conclusions

The ADRE (1) can be approximated by grid-based or PT algorithms. When the advection error is completely eliminated in homogeneous flow conditions, the diffusion and reaction portion of both Eulerian and PT methods converge in an L^1 sense to a "correct" solution. Neither method shows a tendency to converge in a pointwise sense given the limitations of desktop-scale computational resources: as Δx is made smaller or the number of particles made larger, the peak concentrations in the domain tend to rise. This point was not exhaustively investigated but has implications for studies concerned with maximum concentrations within a domain.

As expected, the errors associated with the approximation of advection dominate the behavior of the grid-based simulations. For displacement of one reactant with another starting with square pulse initial conditions, the errors in a classical 1st-order upwind method are remarkably large. The nonlinear interaction of reactants means that this algorithm would need grid Peclet numbers far less than unity to achieve reasonable solutions in terms of integrated product (i.e., total effective reaction rate). Higher-order methods can have spurious over- or under-mixing, depending on the algorithm and shapes of reactant plumes (Appendix A). The 3rd-order algorithm offers potentially the best balance for current Eulerian methods in use, and appears to require classical grid Peclet numbers $\Delta x/\alpha_L \lesssim 10$ for visually acceptable results in heterogeneous velocity fields. The additional computational cost of the 3rd-order method over simple upwind weighting is about 60%, which is certainly justified for the additional accuracy. Quantitatively, when moving from homogeneous to heterogeneous velocities (all other things held equal with a constant $\boldsymbol{D}$) the 3rd-order algorithm produced too much product by about 2% percent (going from 22.1% to 39.4%) relative to PT methods (from 22.1% to 37.3%). This increased reaction due to fluid deformation (17.3% ver-

sus 15.2%) is too great by a factor of 1.14. The grid-based advection error has several interesting effects, including increased volume of reaction, large areas of negative concentrations, and depletion of reactants so that product cannot be formed farther downstream.

The PT methods, whether particle-killing or preserving, have very similar amounts of product produced realization to realization, although the peaks and valleys within single realizations are more pronounced due to the interplay of fluid deformation and concentration fluctuations. Computationally, the particle-killing PT method is, in general, much faster than the grid-based methods for comparable conditions. The particle-preserving algorithm is also faster, but not drastically so, compared to the Eulerian methods. The particle-preserving method is more accurate than any of the studied algorithms, particularly at lower concentrations, and requires fewer realizations to get an estimate of the ensemble average. If initial conditions are known exactly and deterministically, only one Eulerian run is required, so an advantage is found there. It is impossible to directly compare computation times for Eulerian and PT methods, but the former scales with Δx^{d+1}, and the latter with $N/\Delta t$ (particle-killing) to $N^1/\Delta t$ to $N^{1.7}/\Delta t$ (particle-preserving). A new criterion for timestep size $0.25 < 2\sqrt{(8D_m\Delta t)(N(t)/A)} < 3/2$ is proposed (for 2-d), assuming isotropic diffusion. Time steps falling within this range permit enough diffusion to allow sufficiently high collision probabilities while limiting long range, diffusive jumps for a given particle. Additionally, we find that the particle-preserving methods requires that $1 > k_f m_p/(4\pi\sqrt{det(\boldsymbol{D})})$, where m_p is the initial particle mass.

Because of the lack of advection error and favorable computation times, the PT method can be used to examine the subtle changes to local reaction rates that arise in heterogeneous flow fields along with spatially heterogeneous chemical distributions. At present, the particle methods have only been extended to relatively simple reaction chains (e.g., Michaelis–Menton (Ding and Benson, 2015)). Based on the advantages of the PT methods, an examination of further extensions is warranted.

Acknowledgments

The authors thank the six anonymous reviewers for extremely helpful comments. DB and DB received support from NSF grant numbers EAR-1417264, EAR-1351625, EAR-1417264, and EAR-1446236. T.A. gratefully acknowledges support by the Portuguese Foundation for Science and Technology (FCT) under Grant SFRH/BD/89488/2012. D.F-G. received support from MINECO/FEDER under project INDEMNE (#CGL2015-69768-R).

Appendix A. Review of finite-difference schemes

In multiple dimensions, there are several finite volume/finite difference algorithms for scalar transport (see, e.g., (Toro, 2009)). An attractive component of several schemes is the TVD requirement, which eliminates spurious oscillations and is a "single-pass" method. The TVD schemes can be applied in single sequential 1-d sweeps by spatial operator splitting. However, these schemes are 1^{st}-order at best (Toro, 2009). Other schemes can increase the order of convergence accuracy with varying degrees of computational overhead, such as stricter, smaller Courant number criteria, or predictor-corrector type formulations. Toro (2009) provides an excellent overview. Here, for exposition, we choose the TVD methods and show their optimal behavior in 1-d.

For concentrations q, the wave equation $q_t = -v \cdot q_x$ has an Euler approximation at the ith location and the nth timestep of $q_i^n = q_i - (\Delta t/\Delta x)(f_{i+1/2} - f_{i-1/2})$, where f are the fluxes at cell faces. The lack of superscript implies values from the previous $(n-1)$ timestep. In the simplest case of uniform positive velocity in 1-d and constant Δx, this simplifies to $q_i^n = q_i - (v\Delta t/\Delta x)(q_{i+1/2} - q_{i-1/2})$. A first-order upwind or "donor-cell" scheme uses $q_{i-1/2} = q_{i-1}$. Higher-order methods adjust the flux at a cell face to represent the change in concentration over a timestep. This can be derived in several ways (LeVeque, 1992; 2002), including higher-order estimates of the concentration derivatives or predictor-corrector techniques generally referred to as flux corrected transport (FCT) (applications to hydrology problems include (Cirpka et al., 1999; Hills et al., 1994)). We will not investigate the FCT methods here, focusing instead on the efficient one-step TVD methods. The second-order methods use a (linear) estimate of the slope S_i of the concentration in an upwind cell that leads to a change of flux over the timestep. Then integrating the linear change of concentration over a timestep gives a new estimate of the upwind concentration

$$q_{i-1/2} = q_{i-1} + S_{i-1}(\Delta x - v\Delta t)/2 \tag{A.1}$$

$$= q_{i-1} + S_{i-1}\Delta x(1-\lambda)/2 \tag{A.2}$$

A natural choice of slope $S_{i-1} = (q_i - q_{i-1})/\Delta x$ gives the Lax–Wendroff scheme. These calculated slopes will be discontinuous and can lead to overshoot and oscillation, so the amount of allowable flux can be limited according to the values of neighboring slopes. If discontinuities are found, the slopes are adjusted. Replacing $S_{i-1}\Delta x$ in the last Eq. (A.1) with a general function and the difference in the two surrounding known concentrations $\phi(r_{i-1/2})(q_i - q_{i-1})$ gives the flux-limited form

$$q_{i-1/2} = q_{i-1} + \frac{(1-\lambda)}{2}\phi(r_{i-1/2})(q_i - q_{i-1}) \tag{A.3}$$

where $r_{i-1/2} = (q_{i-1} - q_{i-2})/(q_i - q_{i-1})$ is a ratio of upstream and downstream gradients relative to the donor cell $i-1$. Generalizations to variable velocity magnitude and direction are straightforward. For reference, the Lax–Wendroff 2nd-order formula sets $\phi(r) = 1$ and leads to overshoot and oscillation. Various schemes have been developed based on eliminating spurious fluctuations. A common method requires that the total variation of q, given for example by $\int|dq/dx|dx$, must not increase. Given this constraint of total variation diminishment (TVD), and keeping the requirement that the solution be second-order accurate, Sweby (1984) showed that the allowable values of $\phi(r)$ must lie in the shaded area of Fig. A.1. Schemes that follow the bottom of the region are the most diffusive; schemes along the top are least (and can be compressive, leading to overly steep shock fronts). The four limiters shown on the plot – Roe's superbee, (see (Sweby, 1984)), Van Leer (van Leer, 1974), minmod (Roe and Baines, 1982), and Leonard's 3rd-order (Datta-Gupta et al., 1991; Leonard, 1991) – are chosen here to represent the range of behaviors. The first-order upwind scheme uses $\phi(r) = 0$ and can obviously be coded without looking at three nodal concentrations per face and is faster. The 3rd-order solution adjusts the form of $\phi(r)$ based on the local value of λ (Fig. A.1) according to $\phi(r,\lambda) = \max[0, \min\{\min(2, 2r), \frac{1}{3}((2-\lambda) + (1+\lambda)r)\}]$.

For an illustration of the effects of the TVD schemes, the ADRE was coded in 1-d using operator splitting. Parameters were held the same as in Section 4. The number of grid blocks was held at 512, or 1/4 the maximum number used in Section 4, roughly representing equivalent computational effort. For the square-pulse initial condition specified (Fig. 1), the least diffusive flux limiter (superbee) is clearly most accurate over the full range of Courant numbers tested (Fig. A.2). Based on this plot, one might assume that the superbee limiter is best; however, its compressive (anti-diffusive) nature is well suited to discontinuous concentrations. Smoother fields are artificially sharpened. To illustrate, a similar initial condition is specified in which equal, but Gaussian-shaped masses of reactants A and B are placed near each other (Fig. A.3). The total product masses are lower at $\lambda = 1$ because the centers

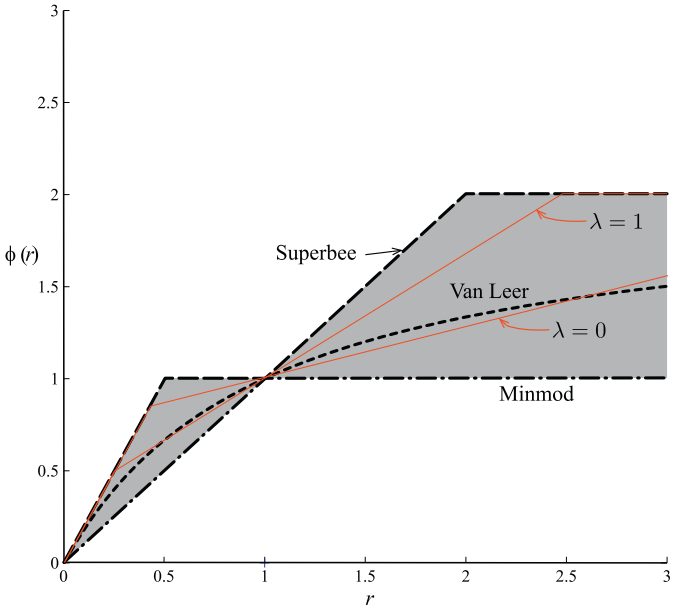

Fig. A1. Region of acceptable TVD flux-limiters (Sweby, 1984). Limiters for this study are the 2nd-order maximally diffusive minmod (dash-dot line), minimally diffusive superbee (large dashes), intermediate Van Leer (small dashes), and Leonard's 3rd-order, which depends on local Courant number and smoothly interpolates the region between $\lambda = [0, 1]$ (red solid lines). (For interpretation of the references to colour in this figure legend, the reader is referred to the web version of this article.)

of A and B mass are farther apart, but it is clear that the superbee limiter is under-predicting the overlap and mixing of the plumes at later times (Fig. A.4). In fact, the reaction for $\lambda = 0.1$ has nearly ceased at the end of the simulation (not shown). Clearly, there is no optimal advection scheme for all types of plumes or mixtures of Courant numbers that will be found in a heterogeneous flow field. It is also important to note that extending the higher-order TVD methods to multiple dimensions is not straightforward. Typically, the higher-order methods are applied sequentially in 1-d sweeps via directional operator-splitting. LeVeque (2002) notes that any method that is TVD in 2-d is, at most, 1st-order accurate, although some multi-dimensional techniques appear to maintain higher-order accuracy in simultaneous multi-dimensional calculations (e.g., (Colella, 1990; Thuburn, 1996)). Performing sequential 1-d sweeps through a multi-dimensional domain is presently the best technique used in water resource applications (especially within readily-available codes), even though that method does not explicitly account for cross-derivatives that naturally come up in the addition of the higher-order anti-diffusion.

Appendix B. Semi-analytical solutions for mass of product produced

Solutions are tractable under two end-member conditions: fast and slow reactions.

B.1. Slow reaction – A perturbation solution approach

In 1-d the ADRE (1) is given by

$$\frac{\partial C_i}{\partial t} + u\frac{\partial C_i}{\partial x} = D\frac{\partial^2 C_i}{\partial x^2} - kC_AC_B \qquad i = A, B \tag{B.1}$$

This equation can be rewritten in dimensionless forms by defining dimensionless variables $t^* = t\frac{u}{l}$, $x^* = x/l$, and $C^* = C/C_{ref}$, where l is a characteristic distance (e.g., the initial width of the plume in our simulations) and C_{ref} is a characteristic concentration (e.g., the initial concentration). For ease of notation we drop the stars and in dimensionless form (B.1) becomes

$$\frac{\partial C_i}{\partial t} + \frac{\partial C_i}{\partial x} = \frac{1}{Pe}\frac{\partial^2 C_i}{\partial x^2} - DaC_AC_B \qquad i = A, B \tag{B.2}$$

where $Pe = \frac{ul}{D}$ is the Peclet number and $Da = \frac{kC_0 l}{u}$ the Damköhler number. We are considering the limit of slow reactions and thus take Da as small. Doing this we can write the following expansion for concentration (Van Dyke, 1975):

$$C_i = \sum_{n=0}^{\infty} C_i^{(n)} Da^n \tag{B.3}$$

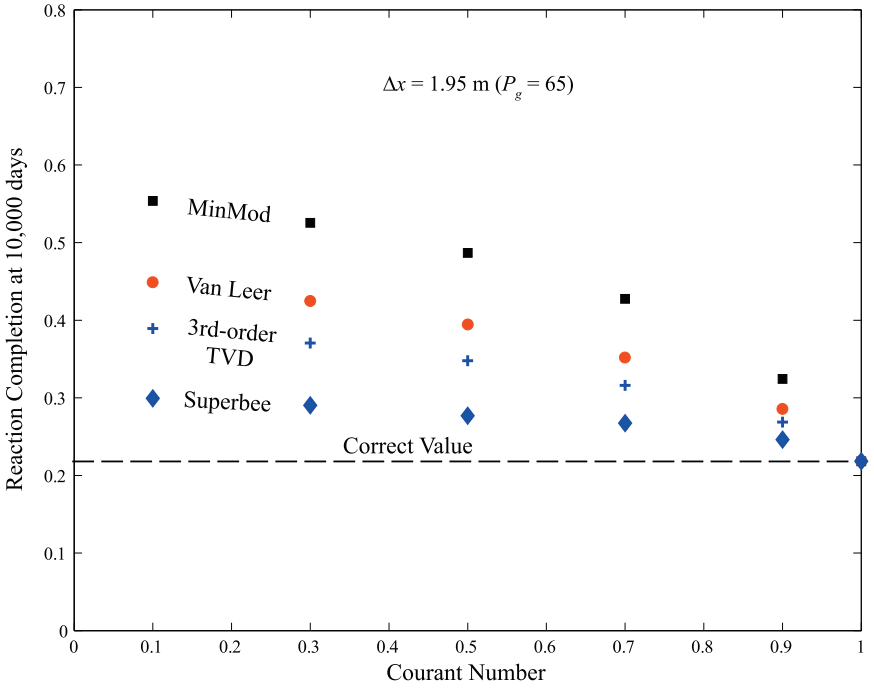

Fig. A2. 1-d solutions to the adjacent square-pulse initial condition problem using different TVD advection schemes.

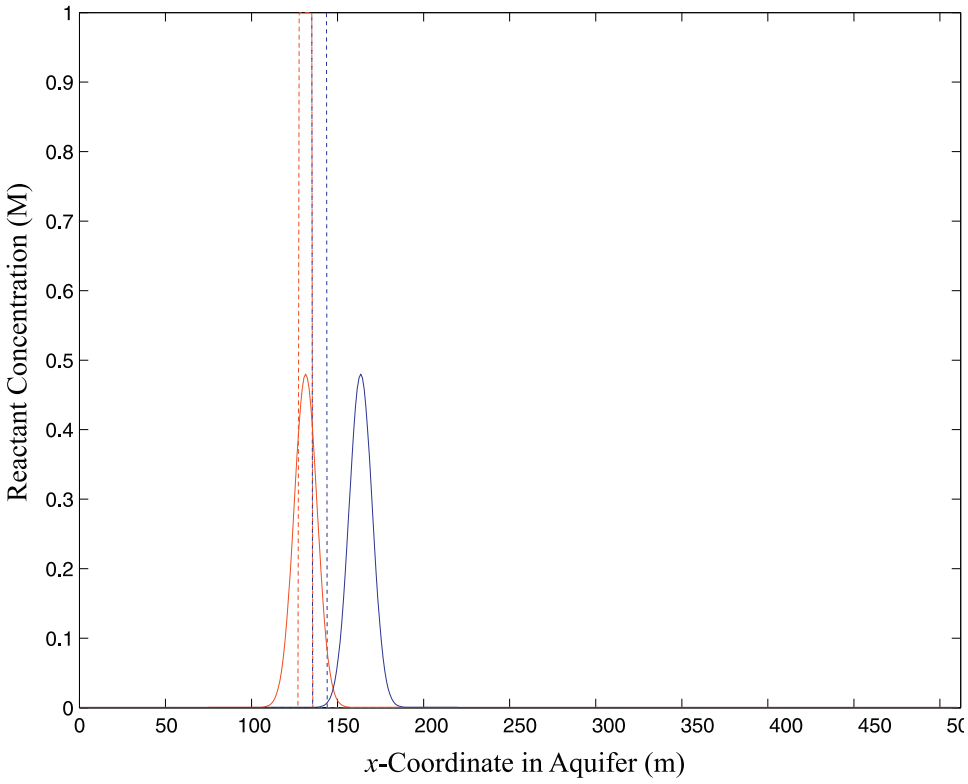

Fig. A3. 1-*d* versions of the two initial conditions of reactants *A* (red) and *B* (blue). The square pulses (dotted) mimic the original 2-*d* simulations in Section 4. An additional set of I.C.s is shown that place identical masses in nearby Gaussian pulses (solid red and blue curves). (For interpretation of the references to colour in this figure legend, the reader is referred to the web version of this article.)

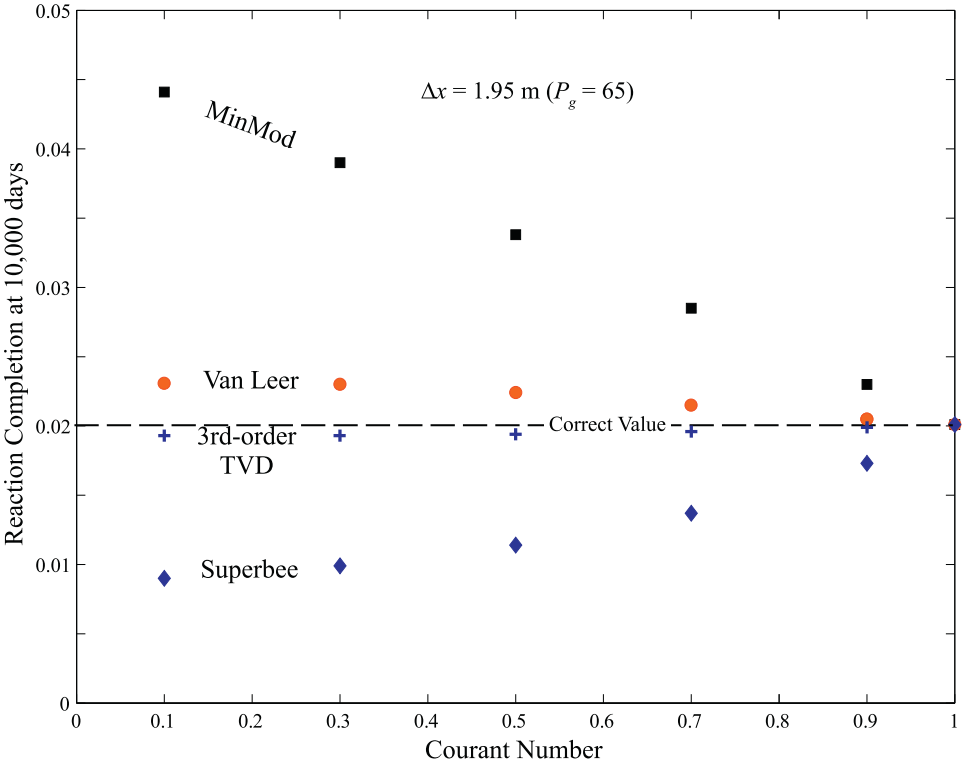

Fig. A4. 1-*d* solutions to the adjacent Gaussian-pulse initial condition problem using different TVD advection schemes.

Then at $O(Da^0)$

$$\frac{\partial C_i^{(0)}}{\partial t}+\frac{\partial C_i^{(0)}}{\partial x}=\frac{1}{Pe}\frac{\partial^2 C_i^{(0)}}{\partial x^2}\qquad i=A,B \tag{B.4}$$

Recognizing that the effect of advection is just a Gallilean shift, we move into a moving reference frame $z=x-t$ and

$$\frac{\partial C_i^{(0)}}{\partial t}=\frac{1}{Pe}\frac{\partial^2 C_i^{(0)}}{\partial z^2}\qquad i=A,B \tag{B.5}$$

In an infinite domain the solution to these equations is given by

$$C_i^{(0)}=\sqrt{\frac{Pe}{4\pi t}}\int_{-\infty}^{\infty}e^{\frac{-(z-\xi)^2 Pe}{4t}}C_i(t=0)d\xi \tag{B.6}$$

At $O(Da^1)$

$$\frac{\partial C_i^{(1)}}{\partial t}=\frac{1}{Pe}\frac{\partial^2 C_i^{(1)}}{\partial z^2}-C_A^{(0)}C_B^{(0)}\qquad i=A,B \tag{B.7}$$

Given this equation and truncating series (B.3) for concentrations at $O(Da^1)$ the total mass of the product will be given by

$$M(t)=Da\int_{-\infty}^{\infty}\int_0^t C_A^{(0)}(z,t')C_B^{(0)}(z,t')dt'dz \tag{B.8}$$

Thus in principle for any initial condition we can now calculate the produced mass to within approximation of the perturbation series. Any error introduced via numerical dispersion will manifest as an error in the concentration fields $C_A^{(0)}(z,t')$ and $C_B^{(0)}(z,t')$ via a modified $Pe=(ul)/(D+D_{numerical})$, which will compound in an error in the resultant product mass.

The nonlinear and initial condition specific nature of the reaction makes it difficult to make general statements on how this error will manifest. For demonstration purposes, consider the following simple example, an infinite domain half filled with A and half filled with B, separated by a sharp interface at $x=0$. At short times (i.e., when the diffusive length is much less than the initial plume width) this mimics the example setups studied in this work. For this setup the initial conditions are given by

$$\begin{aligned}C_A(t=0)&=1 \qquad -\infty<x<0\\ C_B(t=0)&=1 \qquad 0<x<\infty\end{aligned} \tag{B.9}$$

and zero elsewhere, which means

$$C_A^{(0)}(z,t)=\frac{1}{2}\mathrm{erfc}\left[\frac{z\sqrt{Pe}}{\sqrt{4t}}\right]\qquad C_B^{(0)}(z,t)=1-\frac{1}{2}\mathrm{erfc}\left[\frac{z\sqrt{Pe}}{\sqrt{4t}}\right] \tag{B.10}$$

Thus solving (B.8) is trivial and gives

$$M(t)=\frac{2}{3}Da\sqrt{\frac{2}{\pi Pe}}t^{3/2} \tag{B.11}$$

The key feature is that $M(t)\propto\frac{1}{\sqrt{Pe}}$, or in dimensional terms that the mass or product produced is proportional to $\sqrt{D}$. Given that in the Eulerian numerical models the dispersion coefficient will be $D=D_{actual}+D_{numerical}$, any error in the dispersion coefficient induced by numerical dispersion will increase the predicted amount of mass produced in this manner. The results for the specific initial conditions studied in this paper are cumbersome and provide little insight and are thus not shown. However, to leading order it can be shown that the initial condition studied in this paper has the same scaling.

B.2. Fast reactions

Now if we consider the other extreme when Da is large, we can treat the reaction as instantaneous, which in previous studies has been shown to be a good assumption for $Da>10$ (Sanchez-Vila et al., 2007). Under this assumption A and B cannot coexist, meaning that the lesser will be consumed entirely. Now following the development of Gramling et al. (2002), define two conservative pseudo-tracers as

$$U_A=C_A+C_P\qquad U_B=C_B+C_P \tag{B.12}$$

These are governed by a conservative transport equation because upon summation of the ADREs (1) for C_A and C_P, the reaction terms disappear (because A and B disappear at the same rate as P by stoichiometry). For the initial conditions considered in (B.1)

$$\begin{aligned}U_A(t=0)&=1 \qquad -\infty<x<0\\ U_B(t=0)&=1 \qquad 0<x<\infty\end{aligned} \tag{B.13}$$

which means that at all times

$$\begin{aligned}U_A(t)&=\frac{1}{2}\mathrm{erfc}\left[\frac{(x-ut)\sqrt{Pe}}{\sqrt{4t}}\right]\\ U_B(t)&=1-\frac{1}{2}\mathrm{erfc}\left[\frac{(x-ut)\sqrt{Pe}}{\sqrt{4t}}\right]\end{aligned} \tag{B.14}$$

Now since A and B cannot coexist, the concentration of product is given by

$$C_P=\min(U_A,U_B) \tag{B.15}$$

and the total mass of product for the semi-infinite sources (following Gramling et al. (2002)) is given by

$$M=\int_{-\infty}^{\infty}C_P dx=2\int_0^{\infty}U_A dx=2\sqrt{\frac{t}{Pe\pi}} \tag{B.16}$$

A more accurate equation for the finite (in the x-direction) sources is

$$M_C(t)=\sqrt{\frac{4t}{\pi Pe}}(1-e^{-\frac{Pe}{4t}})+1-\mathrm{erf}\left[\sqrt{\frac{Pe}{4t}}\right] \tag{B.17}$$

which recovers (B.16) for $l\to\infty$. The 20,000 particle simulations follow formula (B.17) fairly closely at later time (Fig. B.1) using the intial condition $l=15.6$ m for an estimation of the scaling length. The early time discrepancy is most likely due to the fact that our reactions are not instantaneous, but take some time (albeit small) to develop.

B.3. Slow reactions generalized to a higher order reaction $-kC_A^nC_B^m$

To demonstrate how these effect might be influenced for higher order reactions, consider taking $r=-kC_A^nC_B^m$. Following the same procedures as above for slow reactions (i.e. Appendix B.1) the total mass produced will be

$$\begin{aligned}M(t)=&\int_0^t\int_{-\infty}^{\infty}Da\frac{Pe^{\frac{n+m}{2}}}{(4\pi t')^{\frac{n+m}{2}}}\prod_{i=1}^{n}\int_{-\infty}^{0}e^{\frac{-(x-\xi_i)^2Pe}{4t'}}d\xi_i\prod_{j=1}^{m}\int_0^{\infty}\\ &\times e^{\frac{-(x-\eta_j)^2Pe}{4t'}}d\eta_j dx dt'\end{aligned} \tag{B.18}$$

Now rescale all the length scales by $\sqrt{\frac{Pe}{4t'}}$, i.e.

$$\xi'=\xi\sqrt{\frac{Pe}{4t'}}\qquad \eta'=\eta\sqrt{\frac{Pe}{4t'}}\qquad x=x\sqrt{\frac{Pe}{4t'}} \tag{B.19}$$

Then

$$\begin{aligned}M(t)=&\int_0^t\int_{-\infty}^{\infty}Da\sqrt{\frac{4t'}{Pe}}\frac{1}{\pi^{\frac{n+m}{2}}}\prod_{i=1}^{n}\int_{-\infty}^{0}\\ &\times e^{-(x-\xi_i)^2}d\xi_i\prod_{j=1}^{m}\int_0^{\infty}e^{-(x-\eta_i)^2}d\eta_j dx dt'\end{aligned} \tag{B.20}$$

which gives

$$M(t)=W\frac{2Da}{3}\sqrt{\frac{2}{Pe}}t^{3/2} \tag{B.21}$$

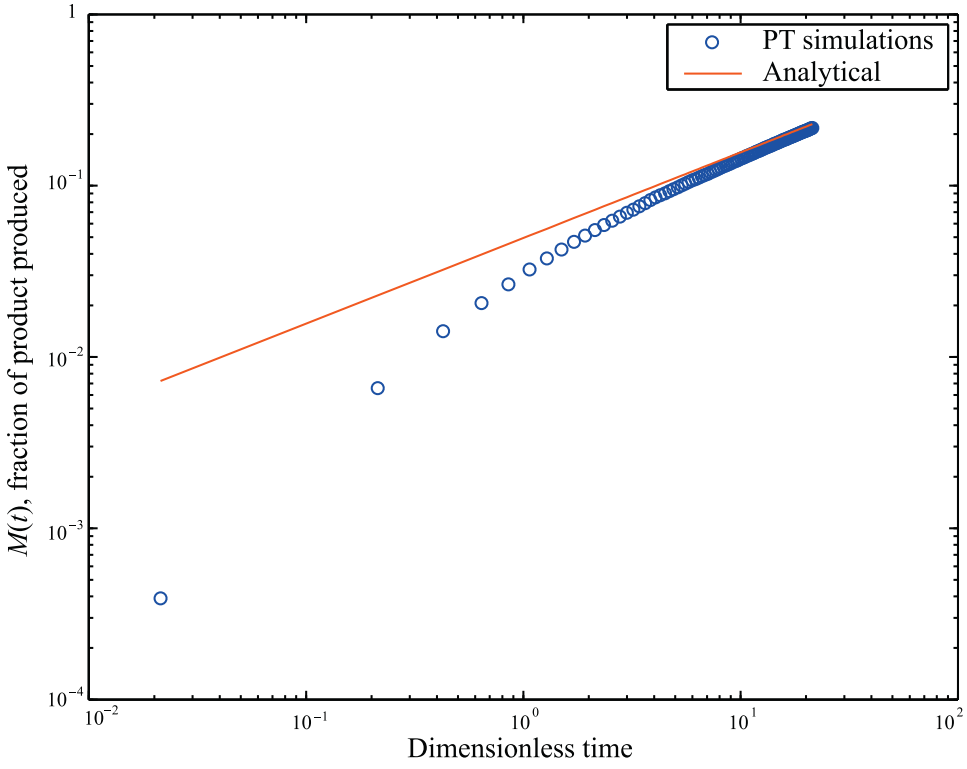

Fig. B1. Evolution of the mass of product in the 20,000 particle simulations in a homogeneous velocity field (symbols), along with the solution to the analytical expression (B.17).

where the constant W is given by

$$W = \frac{1}{\pi^{\frac{n+m}{2}}} \int_{-\infty}^{\infty} \prod_{i=1}^{n} \int_{-\infty}^{0} e^{-(x-\xi_i)^2} d\xi_i \prod_{j=1}^{m} \int_{0}^{\infty} e^{-(x-\eta_i)^2} d\eta_j dx \qquad \text{(B.22)}$$

The specific value of W is unimportant to the central message. From (B.21) we see again that the total amount of mass produced has the same proportionality as before of $M(t) \propto \frac{1}{\sqrt{Pe}}$. At this point it is not clear how to generalize the fast reactions scenario to higher order reactions.

B.4. Error estimates

The foregoing sections of this Appendix show that the mass produced is roughly proportional to $\sqrt{D}$. This allows the construction of some rules-of-thumb for error estimation. The ratio of mass produced with numerical error to mass produced without error is $\sqrt{D_{actual} + D_{numerical}}/\sqrt{D_{actual}}$. Therefore the excess amount of mass produced in error expressed as a fraction of the real amount is $Error = \sqrt{1 + D_{numerical}/D_{actual}} - 1$. For isotropic, fixed D_{actual} in our first-order upwind scheme, we have

$$Error = \sqrt{1 + \frac{|v|\Delta x}{2D_{actual}}(1 - |v|\Delta t/\Delta x)} - 1 \qquad \text{(B.23)}$$

In the case of velocity-dependent dispersion in which the longitudinal dispersion is given by $D_{actual} = \alpha_L |v|$, the error is

$$Error = \sqrt{1 + \frac{\Delta x}{2\alpha_L}(1 - |v|\Delta t/\Delta x)} - 1 \qquad \text{(B.24)}$$

The latter of these two errors is greater for regions of smaller velocity in the domain, as the former goes to zero for $|v| \to 0$. Fig. B.3 shows the magnitude of these two error estimates for reasonable values in the example heterogeneous domain ($\Delta x = 1$ m, $\max(v) = 1.46$ m/d), along with a histogram of the velocities within the (log-normal) K field. For a large portion of the domain experiencing low velocity, the error is greater for a velocity-dependent dispersion.

Appendix C. PT simulation of anisotropic dispersion and reaction.

We solve (1) via PT using operator-splitting as follows: The finite-time discretized Langevin equation applied to each particle's position $\boldsymbol{X}$ for the backward Kolmogorov transport portion of Eq. (1) follows $\boldsymbol{X}_{t+\Delta t} = \boldsymbol{X}_t + (\boldsymbol{v} + \nabla \boldsymbol{D})\Delta t + \boldsymbol{B}W$, where $\boldsymbol{B} = \sqrt{2\Delta t \boldsymbol{D}}$ after $\boldsymbol{D}$ is diagonalized by rotation into a coordinate system along the flow direction, and W is a standard multiGaussian random vector (Labolle et al., 1996).

The velocities are calculated at cell faces following an iterative solution of the continuity equation for constant-density fluid $\nabla \cdot K\nabla h = 0$ followed by $\boldsymbol{v} = -K\nabla h/\theta$. Constant values of h at the left and right boundaries, along with no-flow $\nabla h \cdot \boldsymbol{n} = 0$ along the top and bottom boundaries maintain the desired mean gradient from left to right. The K is constant within each rectilinear volume (cell), porosity θ is constant everywhere, and $\boldsymbol{v}$ is calculated at cell faces and linearly interpolated to each particle's location within the cells. Dispersion components for each particle use these linearly-interpolated velocities. Because the calculation of the gradients of dispersion coefficients at the exact particle location are relatively time consuming by bilinear interpolation (see (Labolle et al., 1996)), we make a simplification that the gradients can be well approximated as constant within each cell. This follows directly from the linear velocity interpolation and linear dispersion dependence on velocity. For example, in 2-d with indices i, j in the x, y-directions, the components D_{xx} and D_{yx} are calculated at the $i-1/2$ and $i+1/2$ faces, while D_{yy} and D_{xy} are calculated at the $j-1/2$ and $j+1/2$ faces. So for the i, j block, $\frac{dD_{xx}}{dx} = (D_{xx}(i+1/2) - D_{xx}(i-1/2))/\Delta x$, $\frac{dD_{yx}}{dx} = (D_{yx}(i+$

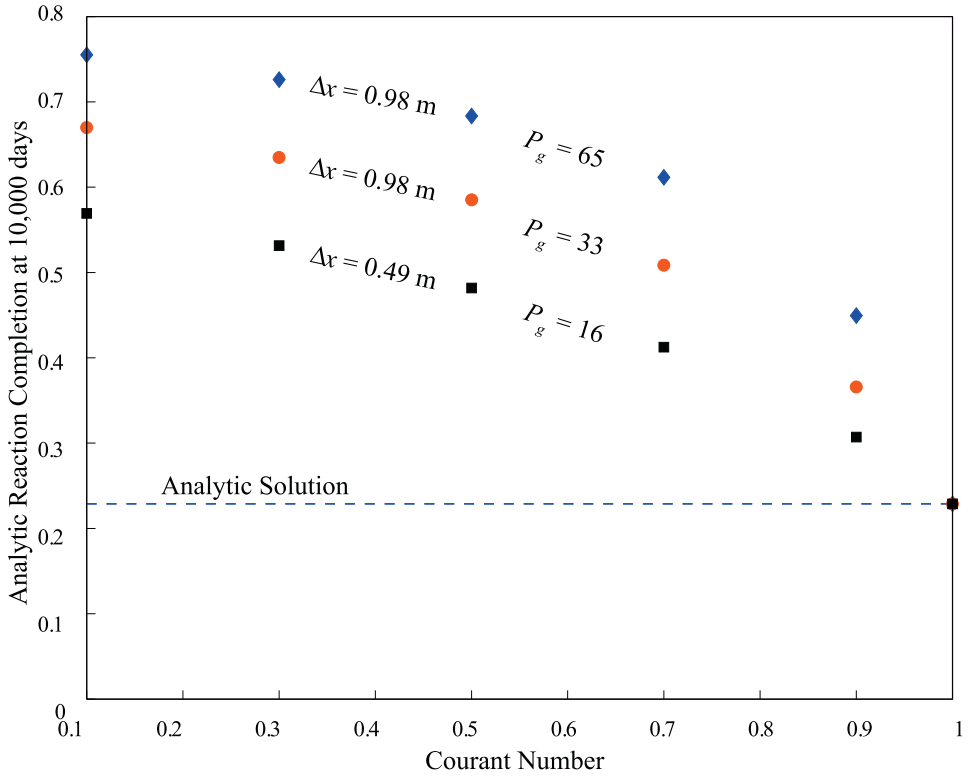

Fig. B2. Analytic solutions (using (B.17)) for mass created at 10,000 days incorporating the errors due to numerical dispersion for the upwind scheme.

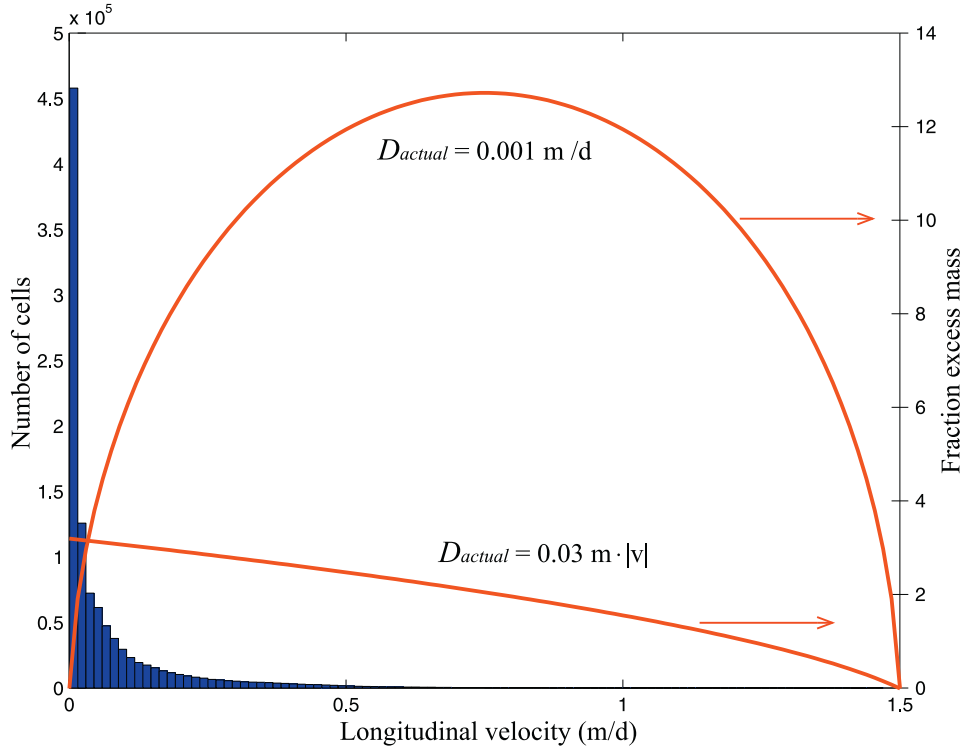

Fig. B3. Histogram (blue bars) of velocity magnitude in the heterogeneous domain pictured in Fig. 8. Estimates of the excess mass production error (red curves) by the upwind advection algorithm as a function of velocty (hence grid Peclet and Courant numbers) for fixed dispersion value 0.001 m^2/d and a velocity-dependent dispersion with $\alpha_L = 0.03$ m. The right-hand labels are for excess error as a multiple of the real production value. (For interpretation of the references to colour in this figure legend, the reader is referred to the web version of this article.)

$1/2) - D_{yx}(i-1/2))/\Delta x$, $\frac{dD_{yy}}{dy} = (D_{yy}(j+1/2) - D_{yy}(j-1/2))/\Delta y$, $\frac{dD_{xy}}{dy} = (D_{xy}(j+1/2) - D_{xy}(j-1/2))/\Delta y$.

In the operator-split method, we enforce zero-diffusive flux BCs in the random walk by reflecting all particles back into the domain (e.g., Salamon et al., 2006b). Particles that move by advection into boundary cells are removed, enforcing $J = \boldsymbol{n}\cdot\boldsymbol{v}C$, where $\boldsymbol{n}$ is the unit normal to the boundary and the relation of concentration to particle mass is thought of as the spatial convolution of any particle's mass with some kernel function with unit integral in d-dimensions. A nice discussion of all types of boundary conditions for advection and dispersion via the PT method is given by Koch and Nowak (2014).

Reactions between particles may either follow the formulas given in (Benson and Meerschaert, 2008) or (Bolster et al., 2016) for particle-killing or particle-preserving methods, respectively. For the latter, each A particle with unique mass $m_A(t)$ at time t is chosen and sequentially subjected to reaction with nearby B particles with unique mass m_B. The change in masses for a single reaction are $dm_A = dm_B = -\Delta t k_f m_B(t) m_A(t) v(\boldsymbol{s})$. Then the net change sums over all reaction partner pairs $m_A(t+\Delta t) = m_A(t) + \sum dm_A$. The co-location density $v(\boldsymbol{s})$ given a separation vector $\boldsymbol{s}$ between an A and B particle pair is given by a multi-Gaussian

$$v(\boldsymbol{s}) = \frac{1}{(8\pi\,\Delta t)^{d/2}|\boldsymbol{D}|^{1/2}} \exp\left(-\frac{1}{8\Delta t}\boldsymbol{s}'\boldsymbol{D}^{-1}\boldsymbol{s}\right). \tag{C.1}$$

The search radius for nearby particles was restricted to $3\sqrt{8\max(D_{ij})\Delta t}$, and the kd-tree algorithm (Bentley, 1975) for nearby particle searching was used as coded in the "rangesearch" algorithm in matlab.

We assume, for calculation speed, that the dispersion tensor is simply that of the "central" A particle. The differences in dispersion tensors between the A and each nearby B particle was ignored, i.e., $\boldsymbol{D} = \boldsymbol{D}_A$. For isotropic dispersion, the above procedure was used with $\boldsymbol{D} = D\boldsymbol{I}$.

References

Apello, C.A.J., Postma, D., 2005. Geochemistry, Groundwater and Pollution, 2nd CRC Press.

Audigane, P., Gaus, I., Czernichowski-Lauriol, I., Pruess, K., Xu, T., 2007. Two-dimensional reactive transport modeling of CO2 injection in a saline aquifer at the Sleipner site, North Sea. Am. J. Sci. 307 (7), 974–1008. http://www.ajsonline.org/cgi/content/abstract/307/7/974.

Avesani, D., Herrera, P., Chiogna, G., Bellin, A., Dumbser, M., 2015. Smooth particle hydrodynamics with nonlinear moving-least-squares weno reconstruction to model anisotropic dispersion in porous media. Adv. Water Resour. 80 (0), 43–59. http://www.sciencedirect.com/science/article/pii/S0309170815000627.

Ayuso, B., Marini, L.D., 2009. Discontinuous Galerkin methods for advection-diffusion-reaction problems. SIAM J. Numer. Anal. 47 (2), 1391–1420.

Bakker, M., Hemker, K., 2004. Analytic solutions for groundwater whirls in box-shaped, layered anisotropic aquifers. Adv Water Resour 27 (11), 1075–1086. http://www.sciencedirect.com/science/article/pii/S0309170804001344.

Barry, D., Prommer, H., Miller, C., Engesgaard, P., Brun, A., Zheng, C., 2002. Modelling the fate of oxidisable organic contaminants in groundwater. Adv Water Resour 25 (8–12), 945–983. http://www.sciencedirect.com/science/article/pii/S0309170802000441.

Battiato, I., Tartakovsky, D.M., 2011. Applicability regimes for macroscopic models of reactive transport in porous media. J. Contam. Hydrol. 120–121, 18–26.

Battiato, I., Tartakovsky, D.M., Tartakovsky, A.M., Scheibe, T., 2009. On breakdown of macroscopic models of mixing-controlled heterogeneous reactions in porous media. Adv. Water Resour. 32, 1664–1673.

Bechtold, M., Vanderborght, J., Ippisch, O., Vereecken, H., 2011. Efficient random walk particle tracking algorithm for advective-dispersive transport in media with discontinuous dispersion coefficients and water contents. Water Resour. Res. 47 (10), W10526. http://dx.doi.org/10.1029/2010WR010267.

Benson, D.A., Carey, A.E., Wheatcraft, S.W., 1998. Numerical advective flux in highly variable velocity fields exemplified by saltwater intrusion. J. Contam. Hydrol. 34, 207–233.

Benson, D.A., Meerschaert, M.M., 2008. Simulation of chemical reaction via particle tracking: diffusion-limited versus thermodynamic rate-limited regimes. Water Resour. Res. 44, W12201. http://dx.doi.org/10.1029/2008WR007111.

Benson, D.A., Meerschaert, M.M., 2009. A simple and efficient random walk solution of multi-rate mobile/immobile mass transport equations. Adv. Water Resour. 32, 532–539.

Benson, D.A., Meerschaert, M.M., Revielle, J., 2013. Fractional calculus in hydrologic modeling: a numerical perspective. Adv. Water Resour. 51 (0), 479–497. http://www.sciencedirect.com/science/article/pii/S0309170812000899.

Bentley, J.L., 1975. Multidimensional binary search trees used for associative searching. Commun. Assoc. Comput. Mach. 18, 509–517.

Bokanowski, O., Zidani, H., 2007. Anti-dissipative schemes for advection and application to Hamilton–Jacobi–Bellmann equations 30 (1), 1–33. http://dx.doi.org/10.1007/s10915-005-9017-0.

Bolster, D., de Anna, P., Benson, D.A., Tartakovsky, A.M., 2012. Incomplete mixing and reactions with fractional dispersion. Adv. Water Resour. 37, 86–93.

Bolster, D., Dentz, M., Borgne, T.L., 2011. Hyper mixing in shear flow. Water Resour. Res. 47, W09602.

Bolster, D., Paster, A., Benson, D.A., 2016. A particle number conserving Lagrangian method for mixing-driven reactive transport. Water Resour. Res. 52 (2), 1518–1527. http://dx.doi.org/10.1002/2015WR018310.

Bolster, D., Valdés-Parada, F.J., LeBorgne, T., Dentz, M., Carrera, J., 2011. Mixing in confined stratified aquifers. J. Contam. Hydrol. 120, 198–212.

Boso, F., Bellin, A., Dumbser, M., 2013. Numerical simulations of solute transport in highly heterogeneous formations: a comparison of alternative numerical schemes. Adv. Water Resour. 52, 178–189.

Burchard, H., Rennau, H., 2008. Comparative quantification of physically and numerically induced mixing in ocean models. Ocean Modell. 20 (3), 293–311. http://www.sciencedirect.com/science/article/pii/S146350030700128X.

Chakraborty, P., Meerschaert, M.M., Lim, C.Y., 2009. Parameter estimation for fractional transport: a particle-tracking approach. Water Resour. Res. 45 (10), W10415. http://dx.doi.org/10.1029/2008WR007577.

Chiogna, G., Bellin, A., 2013. Analytical solution for reactive solute transport considering incomplete mixing within a reference elementary volume. Water Resour. Res. 49 (5), 2589–2600. http://dx.doi.org/10.1002/wrcr.20200.

Chiogna, G., Hochstetler, D.L., Bellin, A., Kitanidis, P.K., Rolle, M., 2012. Mixing, entropy and reactive solute transport. Geophys. Res. Lett. 39 (20).

Chiogna, G., Rolle, M., Bellin, A., Cirpka, O.A., 2014. Helicity and flow topology in three-dimensional anisotropic porous media. Adv. Water Resour. 73 (0), 134–143. http://www.sciencedirect.com/science/article/pii/S0309170814001341.

Cirpka, O.A., de Barros, F.P.J., Chiogna, G., Rolle, M., Nowak, W., 2011. Stochastic flux-related analysis of transverse mixing in two-dimensional heterogeneous porous media. Water Resour. Res. 47 (6), W06515.

Cirpka, O.A., Frind, E.O., Helmig, R., 1999. Numerical methods for reactive transport on rectangular and streamline-oriented grids. Adv. Water Resour. 22 (7), 711–728. http://www.sciencedirect.com/science/article/pii/S0309170898000517.

Cockburn, B., Shu, C., 1998. The local discontinuous Galerkin method for time-dependent convection-diffusion systems. SIAM J. Numer. Anal. 35 (6), 2440–2463.

Colella, P., 1990. Multidimensional upwind methods for hyperbolic conservation laws. J. Comput. Phys. 87 (1), 171–200. http://www.sciencedirect.com/science/article/pii/002199919090233Q.

Constantinescu, E.M., Sandu, A., Carmichael, G.R., 2008. Modeling atmospheric chemistry and transport with dynamic adaptive resolution. Comput. Geosci. 12 (2), 133–151. http://dx.doi.org/10.1007/s10596-007-9065-7.

Datta-Gupta, A., Lake, L.W., Pope, G.A., Sephernoori, K., King, M.J., 1991. High–resolution monotonic schemes for reservoir fluid flow simulation. In Situ 289–317.

de Anna, P., Dentz, M., Tartakovsky, A., Le Borgne, T., 2014. The filamentary structure of mixing fronts and its control on reaction kinetics in porous media flows. Geophys. Res. Lett 41, 4586–4593. http://dx.doi.org/10.1002/2014GL060068.

de Anna, P., Jimenez-Martinez, J., Tabuteau, H., Turuban, R., Le Borgne, T., Derrien, M., Méheust, Y., 2013. Mixing and reaction kinetics in porous media: an experimental pore scale quantification. Environ. Sci. Technol. 48 (1), 508–516.

de Barros, F.P., Dentz, M., 2016. Pictures of blockscale transport: effective versus ensemble dispersion and its uncertainty. Adv Water Resour 91, 11–22. http://www.sciencedirect.com/science/article/pii/S0309170816300549.

de Barros, F.P.J., Dentz, M., Kock, J., Nowak, W., 2012. Flow topology and scalar mixing in spatially heterogeneous flow fields. Geophys. Res. Lett. 39, L08404.

De Simoni, M., Carrera, J., Sanchez-Vila, X., Guadagnini, A., 2005. A procedure for the solution of multicomponent reactive transport problems. Water Resour. Res. 41 (11).

De Simoni, M., Sanchez-Vila, X., Carrera, J., Saaltink, M., 2007. A mixing ratios-based formulation for multicomponent reactive transport. Water Resour. Res. 43 (7).

Dentz, M., Le Borgne, T., Englert, A., Bijeljic, B., 2011. Mixing, spreading and reaction in heterogeneous media: a brief review. J. Contam. Hydrol. 120, 1–17.

Ding, D., Benson, D., Paster, A., Bolster, D., 2012. Modeling bimolecular reactions and transport in porous media via particle tracking. Adv. Water Resour. 53, 56–65. http://dx.doi.org/10.1016/j.advwatres.2012.11.001.

Ding, D., Benson, D.A., 2015. Simulating biodegradation under mixing-limited conditions using Michaelis-Menten (Monod) kinetic expressions in a particle tracking model. Adv. Water Resour. 76, 109–119. http://www.sciencedirect.com/science/article/pii/S0309170814002462.

Doi, M., 1976. Stochastic theory of diffusion-controlled reaction. J. Phys. A Math. Gen. 9, 1479–1495.

Edery, Y., Scher, H., Berkowitz, B., 2009. Modeling bimolecular reactions and transport in porous media. Geophys. Res. Lett. 36 (2), L02407. http://dx.doi.org/10.1029/2008GL036381.

Engdahl, N.B., Benson, D.A., Bolster, D., 2014. Predicting the enhancement of mixing-driven reactions in nonuniform flows using measures of flow topology. Phys. Rev. E 90, 051001. http://link.aps.org/doi/10.1103/PhysRevE.90.051001.

Fernàndez-Garcia, D., Sanchez-Vila, X., 2011. Optimal reconstruction of concentrations, gradients and reaction rates from particle distributions. J. Contam. Hydrol. 120, 99–114.
Gillespie, D.T., 1977. Exact stochastic simulation of coupled chemical reactions. J. Phys. Chem. 81 (25), 2340–2361.
Gillespie, D.T., 2000. The chemical Langevin equation. J. Chem. Phys. 113 (1), 297–306.
Gramling, C., Harvey, C., Meigs, L., 2002. Reactive transport in porous media: a comparison of model prediction with laboratory visualization. Environ. Sci. Technol. 36 (11), 2508–2514.
Hammond, G.E., Lichtner, P.C., 2010. Field-scale model for the natural attenuation of uranium at the Hanford 300 area using high-performance computing. Water Resour. Res. 46 (9), W09527. http://dx.doi.org/10.1029/2009WR008819.
Hansen, S.K., Scher, H., Berkowitz, B., 2014. First-principles derivation of reactive transport modeling parameters for particle tracking and pde approaches. Adv Water Resour 69 (0), 146–158.
Henshaw, W.D., Schwendeman, D.W., 2003. An adaptive numerical scheme for high-speed reactive flow on overlapping grids. J Comput Phys 191 (2), 420–447. http://www.sciencedirect.com/science/article/pii/S0021999103003231.
Herrera, P.A., Valocchi, A.J., Beckie, R.D., 2010. A multidimensional streamline-based method to simulate reactive solute transport in heterogeneous porous media. Adv. Water Resour. 33 (7), 711–727. http://www.sciencedirect.com/science/article/pii/S0309170810000424.
Hills, R.G., Fisher, K.A., Kirkland, M.R., Wierenga, P.J., 1994. Application of flux-corrected transport to the Las Cruces trench site. Water Resour. Res. 30 (8), 2377–2385. http://dx.doi.org/10.1029/94WR01216.
Huang, C.-S., Xiao, F., Arbogast, T., 2015. Fifth order multi-moment weno schemes for hyperbolic conservation laws. J. Sci. Comput. 64, 477–507.
Isaacson, S.A., 2013. A convergent reaction-diffusion master equation. J. Chem. Phys. 139 (5), 054101. http://scitation.aip.org/content/aip/journal/jcp/139/5/10.1063/1.4816377.
Johnson, J.W., Nitao, J.J., Knauss, K.G., 2004. Reactive transport modelling of CO_2 storage in saline aquifers to elucidate fundamental processes, trapping mechanisms and sequestration partitioning. Geolog. Soc. 233 (1), 107–128.
Keating, E.H., Hakala, J.A., Viswanathan, H., Carey, J.W., Pawar, R., Guthrie, G.D., Fessenden-Rahn, J., 2013. CO_2 Leakage impacts on shallow groundwater: field-scale reactive-transport simulations informed by observations at a natural analog site. Appl. Geochem. 30, 136–147. Geochemical Aspects of Geologic Carbon Storage.
Ketcheson, D.I., Parsani, M., LeVeQue, R.J., 2013. High-order wave propagations algorithms for hyperbolic systems. SIAM J. Sci. Comput. 35 (1), A351–A377.
Koch, J., Nowak, W., 2014. A method for implementing dirichlet and third-type boundary conditions in PTRW simulations. Water Resour. Res. 50 (2), 1374–1395. http://dx.doi.org/10.1002/2013WR013796.
Kuzmin, D., 2010. A Guide to Numerical Methods for Transport Equations. Friedrich-Alexander-Universität Erlangen-Nürnberg.
Labolle, E.M., Fogg, G.E., Tompson, A.F.B., 1996. Random-walk simulation of transport in heterogeneous porous media: local mass-conservation problem and implementation methods. Water Resour. Res. 32 (3), 583–593.
Le Borgne, T., Dentz, M., Bolster, D., Carrera, J., De Dreuzy, J.-R., Davy, P., 2010. Non–Fickian mixing: temporal evolution of the scalar dissipation rate in heterogeneous porous media. Adv. Water Resour. 33 (12), 1468–1475.
Le Borgne, T., Dentz, M., Bolster, D., Carrera, J., de Dreuzy, J.-R., Bour, O., 2011. Persistence of incomplete mixing: a key to anomalous transport. Phys. Rev. E 84,„ 015301(R).
Le Borgne, T., Dentz, M., Villermaux, E., 2013. Stretching, coalescence, and mixing in porous media. Phys. Rev. Lett. 110 (20), 204501.
Le Borgne, T., Ginn, T.R., Dentz, M., 2014. Impact of fluid deformation on mixing-induced chemical reactions in heterogeneous flows. Geophys. Res. Lett. 41 (22), 7898–7906. http://dx.doi.org/10.1002/2014GL062038.
van Leer, B., 1974. Towards the ultimate conservative difference scheme. ii. monotonicity and conservation combined in a second-order scheme. J. Comput. Phys. 14, 361–370.
Leonard, B., 1991. The ultimate conservative difference scheme applied to unsteady one-dimensional advection. Comput. Meth. Appl. Mech. Eng. 88 (1), 17–74. http://www.sciencedirect.com/science/article/pii/004578259190232U.
LeVeque, R.J., 1992. Numerical Methods for Conservation Laws. Lectures in Mathematics, 2 ETH Zurich, Birkhauser Verlag.
LeVeque, R.J., 2002. Finite Volume Methods for Hyperbolic Problems. Cambridge University Press.
LeVeque, R.J., 2005. Numerical Methods for Conservation Laws, 2nd edition Birkhäuser.
Lichtner, P.C., Hammond, G.E., Lu, C., Karra, S., Bisht, G., Andre, B., Mills, R.T., Kumar, J., 2013. PFLOTRAN User Manual. Technical Report.
Lv, Y., Ihme, M., 2014. Discontinuous Galerkin method for multicomponent chemically reacting flows and combustion. J. Comput. Phys. 270, 105–137. http://www.sciencedirect.com/science/article/pii/S0021999114002101.
Maier, U., Bürger, C.M., 2013. An accurate method for transient particle tracking. Water Resour. Res. 49 (5), 3059–3063. http://dx.doi.org/10.1002/wrcr.20236.
Mansell, R.S., Ma, L., Ahuja, L.R., Bloom, S.A., 2002. Adaptive grid refinement in numerical models for water flow and chemical transport in soil florida agricultural exp. stn. journal series no. r-08979. 1. http://dx.doi.org/10.2136/vzj2002.2220.
Navarre-Sitchler, A.K., Maxwell, R.M., Siirila, E.R., Hammond, G.E., Lichtner, P.C., 2013. Elucidating geochemical response of shallow heterogeneous aquifers to {CO2} leakage using high-performance computing: implications for monitoring of {CO2} sequestration. Adv. Water Resou.r 53, 45–55. http://www.sciencedirect.com/science/article/pii/S0309170812002679.
Nitao, J.J., 2000. Reference Manual for the NUFT Flow and Transport Code, Version 3.0. Lawrence Livermore National Laboratory.
Oldenburg, C.M., Lewicki, J.L., Dobeck, L., Spangler, L., 2009. Modeling gas transport in the shallow subsurface during the zert co2 release test. Transp Porous Media 82 (1), 77–92. http://dx.doi.org/10.1007/s11242-009-9361-x.
Paster, A., Bolster, D., Benson, D.A., 2013. Particle tracking and the diffusion-reaction equation. Water Resour. Res. 49, 1–6.
Paster, A., Bolster, D., Benson, D.A., 2014. Connecting the dots: semi-analytical and random walk numerical solutions of the diffusion–reaction equation with stochastic initial conditions. J. Comput. Phys. 263 (0), 91–112. http://www.sciencedirect.com/science/article/pii/S0021999114000473.
Pedretti, D., Fernàndez-Garcia, D., 2013. An automatic locally-adaptive method to estimate heavily-tailed breakthrough curves from particle distributions. Adv. Water Resour. 59 (0), 52–65. http://www.sciencedirect.com/science/article/pii/S0309170813000869.
Pollock, D.W., 1988. Semianalytical computation of path lines for finite-difference models. Ground Water 26 (6), 743–750. http://dx.doi.org/10.1111/j.1745-6584.1988.tb00425.x.
Porta, G., Ceriotti, G., Thovert, J.-F., 2016. Comparative assessment of continuum-scale models of bimolecular reactive transport in porous media under pre-asymptotic conditions. J. Contam. Hydrol. 185–186, 1–13. http://www.sciencedirect.com/science/article/pii/S0169772215300474.
Prommer, H., 2006. PHT3D: a reactive multicomponent transport model for saturated porous media. http://www.pht3d.org.
Prommer, H., Barry, D., Davis, G., 2002. Modelling of physical and reactive processes during biodegradation of a hydrocarbon plume under transient groundwater flow conditions. J. Contam. Hydrol. 59 (1–2), 113–131. The 2000 Contaminated Site Remediation Conference: From Source Zones to Ecosystems.
Roe, P.L., Baines, M.J., 1982. Algorithms for advection and shock problems. In: Viviand, H. (Ed.), Proceedings of 4th GAMM conference on Numerical Methods in Fluid Mechanics.
Salamon, P., Fernández-Garcia, D., Gómez-Hernández, J.J., 2006. Modeling mass transfer processes using random walk particle tracking. Water Resour. Res. 42 (11), W11417. http://dx.doi.org/10.1029/2006WR004927.
Salamon, P., Fernàndez-Garcia, D., Gómez-Hernández, J.J., 2006. A review and numerical assessment of the random walk particle tracking method. J. Contam. Hydrol. 87 (3–4), 277–305. http://www.sciencedirect.com/science/article/pii/S0169772206000957.
Sanchez-Vila, X., Dentz, M., Donado, L.D., 2007. Transport-controlled reaction rates under local non-equilibrium conditions. Geophys. Res. Lett. 34 (10).
Sanchez-Vila, X., Fernàndez-Garcia, D., Guadagnini, A., 2010. Interpretation of column experiments of transport of solutes undergoing an irreversible bimolecular reaction using a continuum approximation. Water Resour. Res. 46 (12).
Schwede, R.L., Cirpka, O.A., Nowak, W., Neuweiler, I., 2008. Impact of sampling volume on the probability density function of steady state concentration. Water Resour. Res. 44 (12), W12433.
Smolarkiewicz, P.K., 1984. A fully multidimensional positive definite advection transport algorithm with small implicit diffusion. J. Comput. Phys. 54 (2), 325–362. http://www.sciencedirect.com/science/article/pii/0021999184901219.
Steefel, C.I., 2009. CrunchFlow Software for Modeling Multicomponent Reactive Flow and Transport CrunchFlow CRUNCHFLOW, Software for Modeling Multicomponent Reactive Flow and Transport, USER'S MANUAL. Earth Sciences Division, Lawrence Berkeley National Laboratory, Berkeley, CA.
Steefel, C.I., Appelo, C.A.J., Arora, B., Jacques, D., Kalbacher, T., Kolditz, O., Lagneau, V., Lichtner, P.C., Mayer, K.U., Meeussen, J.C.L., Molins, S., Moulton, D., Shao, H., Šimůnek, J., Spycher, N., Yabusaki, S.B., Yeh, G.T., 2014. Reactive transport codes for subsurface environmental simulation. Comput. Geosci. 19 (3), 445–478. http://dx.doi.org/10.1007/s10596-014-9443-x.
Sweby, P.K., 1984. High resolution schemes using flux limiters for hyperbolic conservation laws. SIAM J. Numer. Anal. 21 (5), 995–1011. http://www.jstor.org/stable/2156939.
Tambue, A., Lord, G., Geiger, S., 2010. An exponential integrator for advection-dominated reactive transport in heterogeneous porous media. J. Comput. Phys. 229 (10), 3957–3969. http://www.sciencedirect.com/science/article/pii/S0021999110000604.
Tartakovsky, A.M., Meakin, P., Scheibe, T.D., Eichler West, R.M., 2007. Simulations of reactive transport and precipitation with smoothed particle hydrodynamics. J. Comput. Phys. 222 (2), 654–672.
Tartakovsky, A.M., Tartakovsky, D.M., Scheibe, T.D., Meakin, P., 2008. Hybrid simulations of reaction-diffusion systems in porous media. SIAM J. Sci. Comput. 30 (6), 2799–2816.
Thuburn, J., 1996. Multidimensional flux-limited advection schemes. J. Comput. Phys. 123 (1), 74–83. http://www.sciencedirect.com/science/article/pii/S0021999196900066.
Tompson, A., Dougherty, D., 1992. Particle-grid methods for reacting flows in porous-media with application to fisher equation. Appl. Math. Model. 16 (7), 374–383.
Toro, E.F., 2009. Riemann Solvers and Numerical Methods for Fluid Dynamics, A Practical Introduction, 3rd edition Springer.
Van Dyke, M., 1975. Perturbation Methods in Fluid Mechanics. Parabolic Press, Stanford.
von Smoluchowski, M., 1917. Versuch einer mathematischen theorie der koagulationskinetik kolloider lösungen. Z. Phys. Chem 92, 124–168.
Werth, C.J., Cirpka, O.A., Grathwohl, P., 2006. Enhanced mixing and reaction through flow focusing in heterogeneous porous media. Water Resour. Res. 42 (12), W12414. http://dx.doi.org/10.1029/2005WR004511.

White, M., Oostrom, M., 1997. STOMP, Subsurface Transport over Multiple Phases, Report Pnnl-11218. Pacific Northwest National Laboratory, Richland, WA.

Wolfsberg, A.V., Freyberg, D.L., 1994. Efficient simulation of single species and multispecies transport in groundwater with local adaptive grid refinement. Water Resour. Res. 30 (11), 2979–2991. http://dx.doi.org/10.1029/93WR02749.

Xu, T., Sonnenthal, E., Spycher, N., Zheng, L., 2014. TOUGHREACT v3.0-OMP Reference Manual: A Parallel Simulation Program for Non-Isothermal TOUGHREACT v3.0-OMP Reference Manual: a Parallel Simulation Program for Non-Isothermal Multiphase Geochemical Reactive Transport, Draft Edition. Earth Sciences Division, Lawrence Berkeley National Laboratory University of California, Berkeley, CA.

Yeh, G.-T., Sun, J., Jardine, P.M., Burgos, W.D., Fang, Y., Li, M.-H., Siegel, M.D., 2004. HYDROGEOCHEM 5.0: A Three-Dimensional Model of Coupled Fluid Flow, Thermal Transport, and HYDROGEOCHEMical Transport through Variably Saturated Conditions: Version 5.0. OAK Ridge National Laboratory.

Zhang, Y., Benson, D.A., Meerschaert, M.M., LaBolle, E.M., Scheffler, H.-P., 2006. Random walk approximation of fractional-order multiscaling anomalous diffusion. Phys. Rev. E 74 (2, Part 2).

Zheng, C., Wang, P.P., 1999. MT3DMS: A modular three-dimensional multispecies transport model for simulation of advection, dispersion and chemical reactions of contaminants in groundwater systems; documentation and user's guide. Contract Report Serdp-99-1 Edition. U.S. Army Engineer Research and Development Center, Vicksburg, MS.

van Zon, J.S., ten Wolde, P.R., 2005. Simulating biochemical networks at the particle level and in time and space: Green's function reaction dynamics. Phys. Rev. Lett. 94 (12), 128103.

Zyvoloski, G., 1997. Summary of the Models and Methods for the FEHM Application – a Finite-Element Heat- and Mass-Transfer Code. Los Alamos National Laboratory Tables, Los Alamos, NM.